Simulation of tsunami induced by a submarine landslide in a glaciomarine margin: the case of Storfjorden SL1 landslide (Southwestern of the Svalbard Islands)

María Teresa Pedrosa-González[1], José Manuel González-Vida [2], Jesús Galindo-Záldivar [1,4], Sergio Ortega[2], Manuel Jesús Castro[3], David Casas[5], Gemma Ercilla[5].

[1]Departamento de Geodinámica, Universidad de Granada, 18071 Granada, Spain.
[2]Departamento de Matemática Aplicada, Escuela de Ingenierías Industriales, Universidad de Málaga, 29071 Málaga, Spain.
[3]Departamento de Análisis Matemática, Estadística e I.O y Matemática Aplicada, Facultad de Ciencias, Universidad de Málaga, 29071 Málaga, Spain.
[4]Instituto Andaluz de Ciencias de La Tierra (CSIC-UGR), Granada, Spain Instituto Andaluz de Ciencias de la Tierra (CSIC-UGR).
[5]Institut de Ciències del Mar, CSIC., 08003 Barcelona, Spain.

Correspondence to: Gemma Ercilla (gemma@icm.csic.es)

Abstract.

A modelling approach to understand the tsunamigenic potentiality of submarine landslides will provide new perspectives on tsunami hazard threat, mostly in polar margins where global climatic change and its related ocean warming may induce future landslides. Here, we use the Landslide L-ML-HySEA numerical model, including wave dispersion, to provide new insights in factors controlling the tsunami characteristics triggered by the Storfjorden SL1 landslide (Southwestern Svalbard). Tsunami waves, determined mainly by the sliding mechanism and the bathymetry, consist of two initial wave dipoles, with troughs to the northeast (Spitsbergen and towards the continent) and crests to the south (seawards) and southwest (Bear Island), reaching more than 3 m of amplitude above the landslide, and finally merging into a single wave dipole. The tsunami wave propagation and its coastal impact are governed by the Kveithola and Storfjorden glacial troughs, and by the bordering Spitsbergen Bank, which shape the continental shelf. This local bathymetry controls the direction of propagation with a crescent shape front, in plan view, and is responsible for shoaling effects amplitude values (-4.2 to 4.3 m), amplification (-3.7 to 4 m), diffraction of the tsunami waves, as well as influencing their coastal impact times.

1 Introduction

Submarine landslides represent one of the most common potential offshore geohazards in the continental slopes of the northern high-latitude margins (Elverhøi et al., 2002; Lee et al., 2009). There, the slope failures are essentially focused at their trough mouth fans (Dowdeswell et al., 2008; Rebesco et al., 2013; Llopart et al., 2016; Ercilla et al., 2022, and references therein). Some landslides may also cause tsunamis, as it has been evidenced in the prehistoric past (Waddington and Wicks et al., 2017), e.g. the striking tsunami caused by the Storegga landslide (3000 km³, at 8.1 ky), that reached the

shore with wave amplitudes of ~20 m (a.s.l.) (Bondevik et al. 2003; Haflidason et al., 2005; Kvalstad et al. 2005), and the
35 Hinlopen landslide (1150 km km^3, at 30 ky) that reached the shore with wave amplitudes of ~40 m (a.s.l.) (Winkelmann et
al., 2008; Vanneste et al., 2006). The factors controlling slope failures in the northern high-latitude margins are still not fully
understood. The most common causal factors are the interlayering of underconsolidated glacially derived sediments and low
permeability interglacial hemipelagic clay rich layers, combined with tectonic and isostatic related seismicity and/or gas
hydrate dissociation (Kvalstad et al., 2005; Canals et al., 2004; Sierro et al., 2009; Garcia et al., 2011; Casas et al., 2013;
40 Vanneste., 2014; Moernaut et al., 2017; Llopart et al., 2019).

   The understanding of the tsunamigenic potentiality of submarine landslides still needs to be improved (Chiocci and
Ridenti, 2011; Løvholt et al., 2020). The modelling of this potentiality, based on past failure analysis, is commonly used to
advance their understanding, as well as to contribute to the hazard assessments of future landslides (Macias et al., 2015;
Rodriguez et al., 2019; Sun and Leslie, 2020; Innocenti et al., 2021). In the European northern high-latitude margins, e.g.
45 Svalbard and Greenland coasts, the tsunami threat has been assessed for a few past landslides. Some examples are the
Hinlopen-Yemark landslide (volume 1150 km^3, at 29.4 ky) in the north of Svalbard, with wave amplitudes of up to ~ 40 m
onshore (Vanneste et al., 2011); and a landslide in the Fram Strait (500 to 1000 km^3), located between the main ice retreat
areas of Greenland and Svalbard, that triggered waves of up to 5.6 m (Berndt et al., 2009). It is important to point out that the
tsunami geohazard of large Holocene structures such as the Bjørnøyrenna (Laberg and Vorren, 1993), which is the largest
50 landslide (volume of about 1100 km^3) in the Barents Sea continental margin, the Nyk landslide in central Norway (Lindberg et
al., 2004), or the giant Andøya landslide (north-eastern Norwegian–Greenland Sea) that covers an area of about 9.700 km^2
(Bugge et al., 1987; Laberg et al 2000), have not been accurately modelled. The tsunami modeling of subrecent landslides in
this region is important, because it will allow us to infer the potentiality of future landslides due to climate change and its
related ocean warming. Both those interconnected issues are significantly affecting the northern high latitude margins, and
55 may contribute to an increase in the occurrence of submarine landslides, both large and small, in the nearby future, mostly
supported by gas hydrate dissociation and rebound related earthquakes (Maslin et al., 1998; Tappin, 2010; Urlaub et al.,
2014). This would result in that region of the planet obtaining a potentially high-risk natural hazard factor.

   Today, the archipelago of Svalbard is one the fastest warming areas of the Arctic Ocean, experiencing an increase
in the melting of their glaciers and a rise in the temperature of ocean water circulating along their continental margin
60 (Meleshko, et al., 2004; Førland et al., 2013; Skogseth, 2020). This fact may provide adequate conditions to trigger
unloading earthquakes, and to increase pore water pressure by gas hydrate breakdown, which destabilizes their slope
sediments (Solheim et al., 2005; Berndt et al., 2009), i.e., the occurrence of landslides and tsunamis in the near future. Both
landslides and tsunamis may represent a danger to offshore infrastructures, such as present and future hydrocarbons
exploitation and other renewable energies such as the wind-sea farms (Zhang et al., 2019). Tsunamis may also have an
65 impact on the coastal areas of the nearby regions of NW Europe, where the population growth is concentrated close to the
sea, due to changes in demographics (Imamura et al., 2019). The geological record of the Svalbard continental margin can
help us assess the possible tsunamis induced by future landslides. In fact, the sedimentary record of its continental slope is

affected by numerous landslides, such as the Storfjorden SL1 landslide, which forms part of a Storfjorden trough mouth fan, and even other recent landslides located in the interfan area of the Storfjorden and Kveithola trough mouth fans (TMFs) (Pedrosa et al., 2011; Rebesco et al., 2012; Lucchi et al., 2012; Llopart al 2015).

In this work, we analyze the tsunamigenic potential of the relative medium-size Storfjorden SL1 landslide to provide new insights in factors controlling tsunami wave characteristics, and their evolution, which will help to better understand the perspectives on tsunami hazard assessment in polar margins. Geomorphic and geotechnical data have been integrated in the L-ML-HySea landslide tsunamigenic model simulating landslide dynamics, tsunami wave generation, propagation and coastal impact.

2 Geological Setting

The Svalbard is located west of the epi-continental Barents Sea and Norwegian continental margin, (Fig. 1a). The archipelago resulted from the opening of the northern Atlantic, a process associated to the formation of major NW-SE fault zones, such as the Knipovich Ridge, the Hornsund Fault Zone (HFZ) crossing the Spitsbergen Island, located south of Barents (Worsley, 1986; Eiken et al., 1994; Engen et al., 2008; Faleide et al., 2008), (Fig. 1b). The post-rift activity of these fault zones has contributed to deform the Plio-Pleistocene sedimentary sequence (Faleide et al., 1993, 2008; Fiedler and Faleide., 1996). These fault zones have been reactivated by isostatic loading and unloading rebound periods (Pirli et al, 2013; Newton and Huuse, 2017) that are responsible for the local seismicity in the continental margin, and can become the trigger of slope failures (Hampel et al., 2009; L'Heureux et al., 2013; Bellwald et al., 2016). Historical earthquakes with magnitudes up to $M_w \sim 5$ have been registered (Auriac et al., 2016), (Fig. 1c).

The northwestern Barents continental slope is affected by the Storfjorden and Kveithola trough mouth fans (TMFs), (Fig. 2), created by the high sediment input from the Storfjorden and Kveithola glacial troughs crossing the continental shelf, during the onset of the major Northern Hemisphere Glaciations, around 2.6-2.7 Ma (Faleide et al., 1996; Butt et al., 2000; Knies et al., 2009). The Storfjorden TMF seafloor is shaped by the relatively large and striking Storfjorden landslide (SL1) , that extends from the shelf-edge to the lower continental slope. In spite of their fresh morphological expression, the seismic stratigraphy indicates that SL1 , (Fig 3) is a palaeolandslide above the 0.2 Ma R1 reflector (Rebesco et al., 2012), that is then draped by a regional 100 ms (~ 10 m) thick sediment unit (Llopart et al., 2015). The SL1 sliding mass is a subtabular depositional body, between 3 and 5 ms thick (Pedrosa et al., 2011).

EGU Open Access
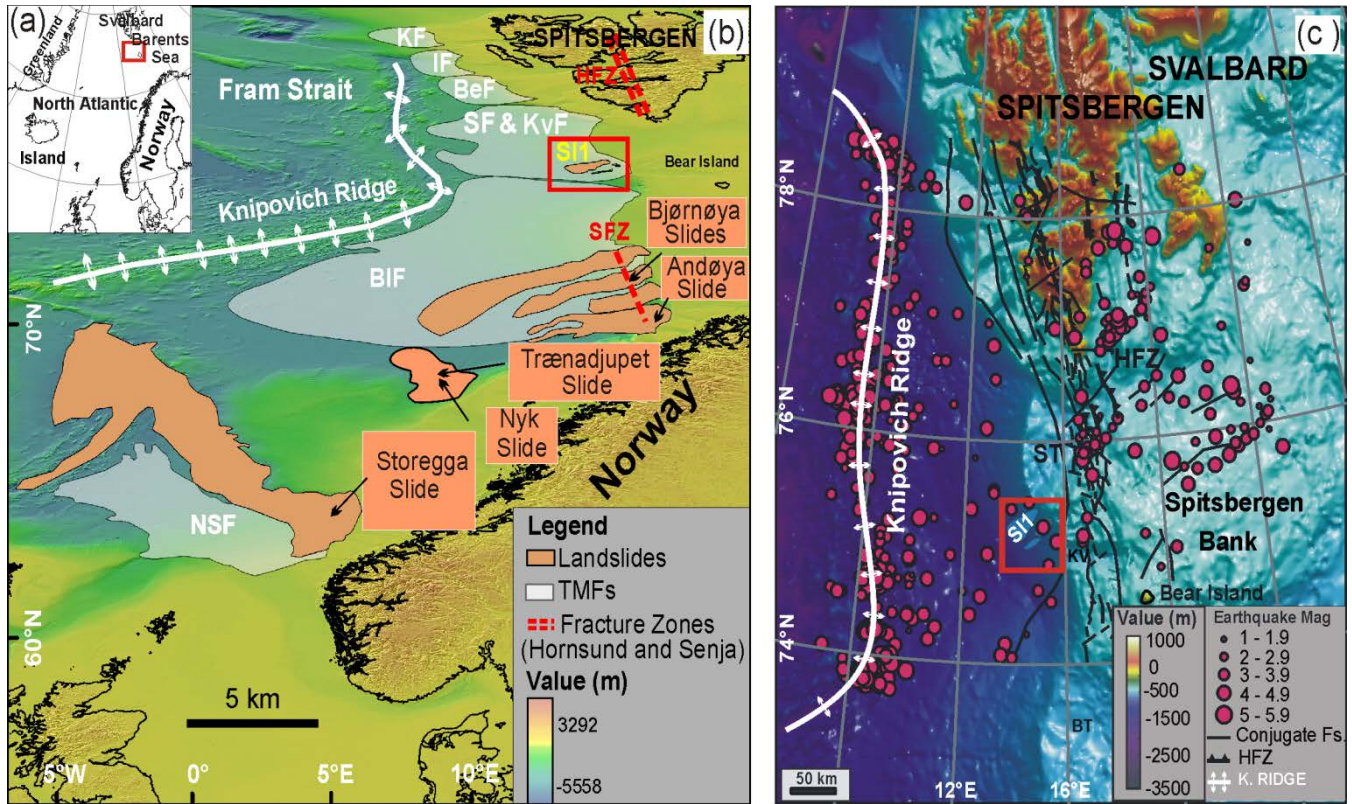
Figure 1. (a) The study area location map (inset). The red rectangle indicates the position of the Storfjorden SL1 landslide and (b) shade relief map taken from the International Bathymetric Chart of the Arctic Ocean (IBCAO) version 3.0 (Jakobsson et al., 2012) of North Atlantic Ocean (Norwegian and Barents Sea). The major Trough Mouth Fans (grey polygons), and the major submarine landslides (orange polygons) are located in the map. Compilation from Haflidason et al. (2005); Laberg et al. (2000); Laberg and Vorren, (2000, 1993); Lindberg et al. (2004); Sejrup et al. (2005), and references therein. KF: Kongsfjorden Fan; IF: Isfjorden Fan; BeF: Bellsund Fan; SF & KvF Storfjorden and Kveithola Fans; BIF: Bear Island Fan; NSF: North Sea Fan. In (c) colour shaded relief map of northwestern Barents Sea from Ottessen et al. (2016) and the historical earthquakes record from 1960 to 2018 (source from IRIS catalogue).

3 Dataset and Methods

3.1. Bathymetric data

High-resolution multibeam bathymetry datasets from different cruises (SVAIS onboard *BIO Hésperides*, 2007; and EGLACOM onboard *R/V Explora* 2008) have been integrated in Figure 2. Data processing consisted of cleaning and filtering the navigation data, noise reduction, and data editing using Caris HIPS SIPS software. Data were gridded at 25 m

and partially cover the Storfjorden-Kveithola TMFs (~15,300 km^2). The bathymetric mosaic was completed with lower

115 resolution bathymetry data provided by Norwegian Hydrography Survey (NHS); these were collected between 1965 and

1985 (Ottessen et al 2006). Gridded bathymetry data for the Arctic Ocean area (IBCAO; https://gebco.net) were also used,

interpolated to 2.5 km bin size.
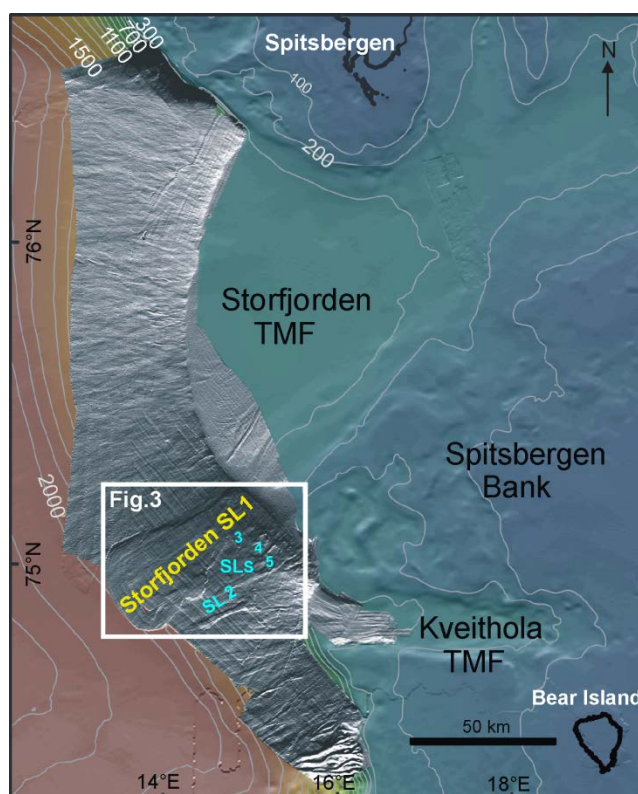
120 **Figure 2.** Shade relief bathymetry map that corresponds to the Storfjorden TMF. It results from the merging of regional low resolution data-set (colour map of 500 m; Ottesen 2006.), and high resolution data-set (75 m) of the Storfjorden and Kveithola TMFs.

3.2. Tsunami numerical modeling

The L-ML-HySEA is a mathematical model, which implements a two-phase model to reproduce the interaction between the

125 landslide granular material (submarine) and the fluid. In the present work, a multilayer non-hydrostatic shallow-water model

is considered in order to model the evolution of the ambient water, taking into account dispersive water waves (Fernández-

Nieto et al., 2018), and to simulate the kinematics of the Storfjorden SL1 submarine landslide using the Savage-Hutter model

(Eq. 3) (Fernando-Nieto et al., 2008).

The L-ML-HySEA model was validated using laboratory experiment data for landslide-generated tsunamis. A
130 milestone in the validation process of this code, consisted in the numerical simulation of the Lituya Bay 1958 mega tsunami
with real topo-bathymetric data obtained from González-Vida et al. (2019). The simulation was also used to generate initial
conditions for the MOST model, in order for it to be initialized for the landslide-generated tsunami scenarios of the
(NTHMP) mandatory benchmarks in the U.S.A. (EDANYA Group, 2015).

L-ML-HySEA needs to incorporate the physical properties of the sediment involved in the landslides. In the
135 Storfjorden (SL1) case, properties determined by Lucchi et al. (2013) and Llopart et al. (2019) were used. For the purposes
of modelling, we have assumed that the landslide took place in a single event. The simulation has been performed by
considering a ~ 1.3° critical slope repose angle, since that value has given the best results across the models.
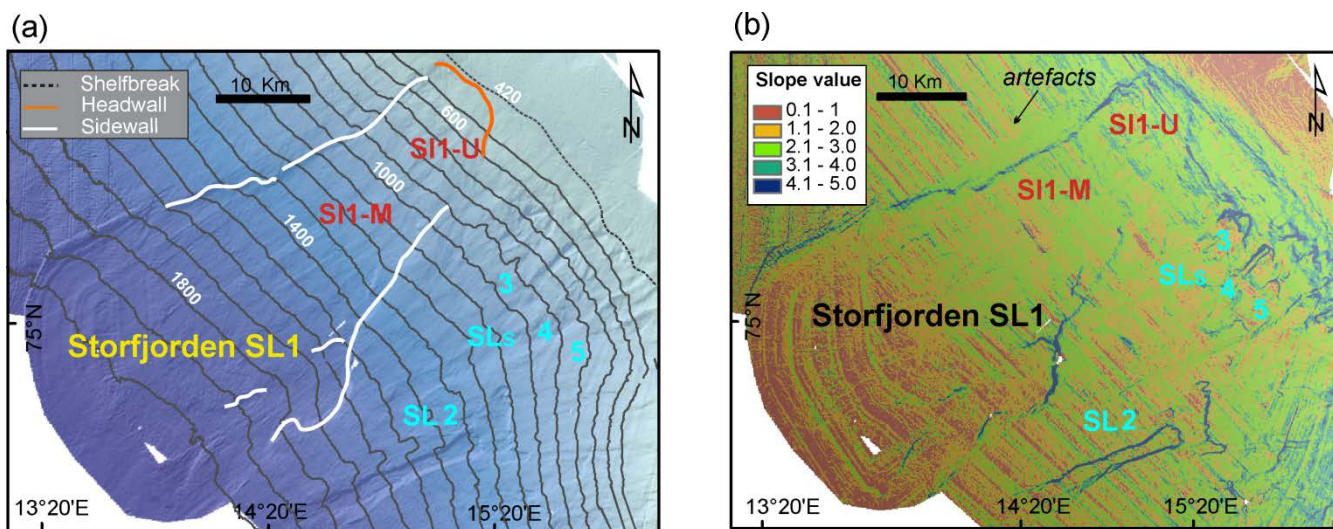
140

Figure 3. (a) The colour-scale bathymetry of the southwestern continental slope of the Storfjorden TMF, results from data
set 70 meters of resolution (Pedrosa et al., 2011). In (b) is represents the slope gradient of the same area imaged in (a)
(illumination from N240°, incidence angle 60°), artefacts are induced by slope parallel the ship tracks.

145 **3.2.1. Reconstruction of pre-landslide bathymetry and landslide body geometry**

To perform the L-ML-HySEA numerical simulation, it is necessary to reconstruct the palaeo-bathymetric scenario as it was
before the seafloor failure (Macías et al., 2015). For that purpose, we used the high-resolution multibeam bathymetry,
together with seismic geometry, to define the landslide location, its body geometry, and buried thickness. We assume that the
sedimentary infill thickness (100 ms; Llopart, et al., 2015) is roughly similar inside and outside of the landslide, and then the
150 present-day bathymetry reproduces the palaeo-bathymetry at 100 ms difference.

The palaeo bathymetry, prior to the Storfjorden SL1, (Fig. 4a) has been calculated by filling the current headwall
and lateral scarps areas using the cartographic sewing technique on the bathymetry with B-Splines (Lee et al., 1997), and
defining a network of B-spline patches (Eck and Hoppe, 1996). The corresponding control vertices splines were developed
using CAD software tools through contour lines from the DEM (Digital Elevation Model) and defined by a tolerance
155 rectangle. When creating the spline, the tolerance rectangle is displayed in the form of construction lines. The control
vertices of the rectangle, which are shown as circles, influence the spline curves. The spline is tangent to the tolerance
rectangle at the start and end points. In this way, the curve ends up adapting to the hypothetical geometry that best fits each
patch. Once the splines were developed, patches were densified through the existing DEM and the points calculated through
the splines, generating a new complete DEM without patches. This procedure uses only data points that are not affected by
160 the landslide, and assumes convergence of both data sets (boundary conditions), where the slide scars terminate. A second
step involves obtaining the volume of the slid sediment body, (Fig. 4b) by calculating the difference between the
reconstructed pre-landslide bathymetry and post-landslide one.
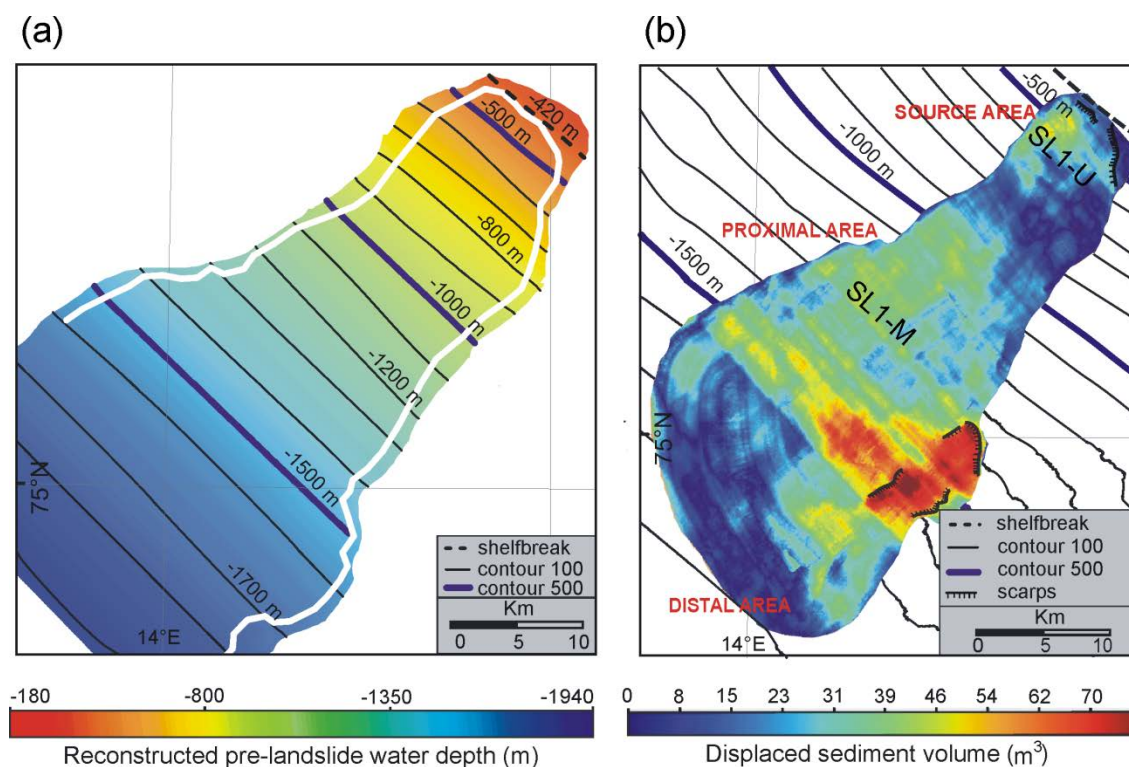
Figure 4. (a) Reconstruction of the landslide area to a hypothetical previous scenario, the cartographic sewing technique
165 using B-Splines has been used (Lee, S. et al., 1997). Contour black lines 500 m (bold) and 100 m (medium). (b) Sediment
volume displaced from the slide-scar area (1300 km^2). Note the location of the different sliding upper and middle sectors
(Sl1-U) and (Sl1-M).

3.2.2. The L-ML-HySEA model equations and discretization

170   The Multilayer-HySEA model consists of a two-phase model that represents the interaction between a submarine or subaerial landslide (composed by granular material) and the ambient fluid. A multi-layer non-hydrostatic shallow-water model, (1) was used for modeling the evolution of the ambient water (see Fernández- Nieto et al., 2018), and the Savage-Hutter model was used for simulating the kinematics of the submarine landslide (2).

175

$$S-W \ system \begin{cases} \partial_t h + \partial_x(hu) = 0, \\ \partial_t(hu) + \partial_x\left(hu^2 + \frac{1}{2}gh^2\right) - gh\partial_x(H - z_s) = n_a(u_s - u), \end{cases} \tag{1}$$

$$S-H \ system \begin{cases} \partial_t z_s + \partial_x(z_s u_s) = 0, \\ \partial_t(z_s u_s) + \partial_x\left(z_s u_s^2 + \frac{1}{2}g(1-r)z_s^2\right) - g(1-r)z_s\partial_x H = -rn_a(u_s - u) + \tau_P. \end{cases} \tag{2}$$

Here, g is the gravity acceleration ($g = 9.81 \, m/s^2$); $H(x)$ is the non-erodible bathymetry measured from a
180   predetermined reference level; $z_s(x,t)$ denotes the thickness of the layer of granular material at each point x at time t; $h(x,t)$ is the total water depth; $\eta(x,t)$ represents the free surface (measured from the same aforementioned fixed reference level) and is given by $\eta = h + z_s - H$. $u(x,t)$ and $u_s(x,t)$ are the averaged horizontal velocity for the water and for the granular material, respectively, and $r = \frac{\rho_1}{\rho_2}$ is the ratio of densities between the ambient fluid and the granular material. The friction between the fluid and the granular layer is parameterized with the term $n_a(u_s - u)$. Finally, $\tau_P(x,t)$ represents the
185   friction between the granular slide and the non-erodible bottom surface. The parameterization follows the system proposed in Pouliquen and Forterre (2002).

These two models are coupled through the boundary conditions at their interface. The parameter r represents the ratio of densities between the ambient fluid and the granular material (slide liquefaction parameter).

Usually, it is formulated that
190
$$r = \frac{\rho_f}{\rho_b}, \rho_b = (1-\varphi)\rho_s + \varphi\rho_f, \tag{3}$$

where ρ_s represents the typical density of the granular material and ρ_f is the density of the fluid ($\rho_s > \rho_f$), both considered constant, and φ represents the porosity ($0 \le \varphi < 1$). In this model φ is supposed to be constant in space and time and, consequently, the ratio r is also constant. This ratio, r, ranges from 0 to 1 (i.e. $0 < r < 1$) and is a value difficult to estimate even in a uniform material, as it depends on the porosity (and ρ_f and ρ_s are also supposed constant) (Fig. 5).

195

3.2.2.1. The fluid model

The ambient fluid is modeled by a multi-layer non-hydrostatic shallow-water system (Férnandez-Nieto et al., 2018), so that dispersive water waves can be taken into account. The model is obtained by a process of depth-averaging of the Euler equations, and can be interpreted as a semi-discretization with respect to the vertical coordinate.

The total pressure is decomposed into the sum of hydrostatic and non-hydrostatic components, in order to take into account dispersive effects. In this process, the horizontal and vertical velocities are supposed to have constant vertical profiles. The resulting multi-layer model admits an exact energy balance, and when the number of layers increases, the linear dispersion relation of the linear model converges to the same of Airy's theory. Finally, the model proposed in (Férnandez-Nieto et al., 2018) can be written in compact form as:

$$\{\partial_t h + \partial_x(hu) = 0, \partial_t(hu_\alpha) + \partial_x\left(hu_\alpha^2 + \frac{1}{2}gh^2\right) - gh\partial_x(H - z_s) + u_{\alpha+1/2}\Gamma_{\alpha+1/2} - u_{\alpha-1/2}\Gamma_{\alpha-1/2}$$
$$= -h(\partial_x p_\alpha + \sigma_\alpha \partial_z p_\alpha) - \tau_\alpha \ \partial_t(hw_\alpha) + \partial_x(hu_\alpha w_\alpha) + w_{\alpha+1/2}\Gamma_{\alpha+1/2} - w_{\alpha-1/2}\Gamma_{\alpha-1/2}$$
$$= -h\partial_z p_\alpha, \partial_x u_{\alpha-1/2} + \sigma_{\alpha-1/2}\partial_z u_{\alpha-1/2} + \partial_z w_{\alpha-1/2} = 0,$$

$$(4) \hspace{8cm} (4)$$

for $\alpha \in \{1,2,\dots,L\}$, with L the number of layers and where the following notation has been used:

$$f_{\alpha+1/2} = \frac{1}{2}(f_{\alpha+1} + f_\alpha), \partial_z f_{\alpha+1/2} = \frac{1}{h\Delta s}(f_{\alpha+1} - f_\alpha),$$

where f denotes one of the generic variables of the system, i.e., u, w and p; $\Delta s = 1/L$ and,

$$\sigma_\alpha = \partial_x\big(H - z_s - h\Delta s(\alpha - 1/2)\big), \sigma_{\alpha-1/2} = \partial_x\big(H - z_s - h\Delta s(\alpha - 1)\big).$$

Schematic picture of model configuration, where the total water height h is decomposed along the vertical axis into $L \geq 1$ layers, (Fig. 5). The depth-averaged velocities in the x and z directions are written as u_α and w_α, respectively. The non-hydrostatic pressure at the interface $z_{\alpha+1/2}$ is denoted by $p_{\alpha+1/2}$. The free surface elevation measured from a fixed reference level (for example the still-water level or mean level in the ocean) is written as η and $\eta = h - H + z_s$, where again $H(x)$ is the unchanged non-erodible bathymetry measured from the same fixed reference level. $\tau_\alpha = 0$, for $\alpha > 1$ and τ_1 is given by

$$\tau_1 = \tau_b - n_a(u_s - u_1),$$

where τ_b stands for a classical Manning-type parameterization for the bottom shear stress and, in this model, is given by

$$\tau_b = gh\frac{n^2}{h^{4/3}}u_1 \vee u_1 \vee,$$

and $n_a(u_s - u_1)$ accounts for the friction between the fluid and the granular layer. The latest two terms are only present at the lowest layer ($\alpha = 1$). Finally, for $\alpha = 1, \dots, L - 1$, $\Gamma_{\alpha+1/2}$ parameterizes the mass transfer across interfaces, and those terms are defined by

225

$$\Gamma_{\alpha+1/2} = \sum_{\beta=\alpha+1}^{L} \partial_x \left(h \Delta s (u_\beta - \overline{u}) \right), \overline{u} = \sum_{\alpha=1}^{L} \Delta s u_\alpha$$

Here we suppose that $\Gamma_{1/2} = \Gamma_{L+1/2} = 0$, which means that there is no mass transfer through the sea-floor or the water free-surface. To close the system, the boundary condition

$$p_{L+1/2} = 0,$$

is imposed at the free surface, and the boundary conditions

230

$$u_0 = 0, w_0 = -\partial_t(H - z_s),$$

are imposed at the bottom. The last two conditions enter into the incompressibility relation for the lowest layer ($\alpha = 1$), given by

$$\partial_x u_{1/2} + \sigma_{1/2} \partial_z u_{1/2} + \partial_z w_{1/2} = 0.$$

It is to be noted that the hydrodynamic model described here and the morphodynamic model described in the next

235 subsection, are coupled through the unknown z_s, that, in the case of the model described here, it is present in the equations and in the boundary condition ($w_0 = -\partial_t(H - z_s)$).

Some dispersive properties of the system (4) were originally studied in (Férnandez-Nieto et al., 2018). Moreover, for a better-detailed study on the dispersion relation (such as 'phase velocity', 'group velocity', and 'linear shoaling') the reader is referred to the work of Macías et al. (2020).

240 Along the derivation of the hydrodynamic model presented here, the rigid-lid assumption for the free surface of the ambient fluid was adopted. Therefore, pressure variations induced by the fluctuation on the free surface of the ambient fluid over the landslide are neglected.
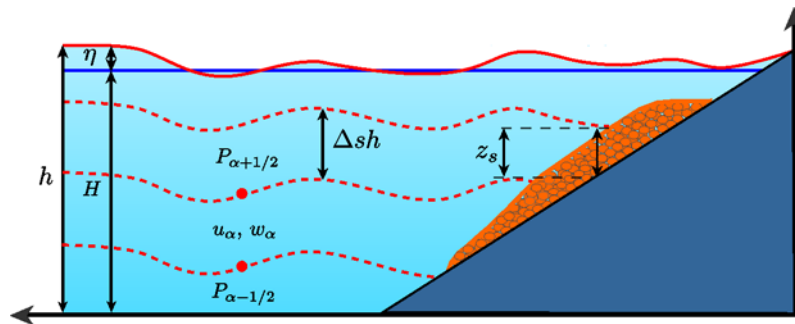
245

Figure 5. The schematic figure to describe the multilayer system.

3.2.2.2. The landslide model

250   The 1D Savage-Hutter method implemented in the model is given by the system (2). The friction law τ_P (Pouliquen and Forterre, 2002) is given by the expression,

$$\tau_P = -g(1-r)\mu z_s \frac{u_s^2}{u_s V,}$$

where μ is a constant friction coefficient with a fundamental role, because it controls the movement of the landslide. Usually μ is given by the Coulomb friction law as it is the simplest parameterization that can be used in landslide models.
255   However, it is well known that a constant friction coefficient does not allow models to reproduce the steady uniform flows over rough beds that are observed in the laboratory for a range of inclination angles. In the work of Pouliquen and Forterre, (2002), in order to reproduce these flows, the authors introduced an empirical friction coefficient μ that depends on the norm of the mean velocity u_s, on the thickness z_s of the granular layer, and on the Froude number $Fr = \frac{u_s}{\sqrt{g z_s}}$. The friction law is given by:

260
$$\mu(z_s, u_s) = \begin{cases} \mu_{start}(z_s) + \left(\frac{Fr}{\beta}\right)^\gamma \left(\mu_{stop}(z_s) - \mu_{start}(z_s)\right), & for Fr < \beta, \\ \mu_{stop}(z_s), & for \beta \leq Fr, \end{cases}$$

with

$$\mu_{start}(z_s) = tan(\delta_3) + \left(tan(\delta_2) - tan(\delta_1)\right)exp\left(\frac{-z_s}{d_s}\right)$$

$$\mu_{stop}(z_s) = tan(\delta_1) + \left(tan(\delta_2) - tan(\delta_1)\right)exp\left(\frac{-z_s \beta}{d_s Fr}\right)$$

265   where d_s represents the mean size of the grains. $\beta = 0.136$ and $\gamma = 10^{-3}$ are empirical parameters. $tan(\delta_1), tan(\delta_2)$ are the characteristic angles of the material, and $tan(\delta_3)$ is another friction angle related to the behavior when starting from rest. This law has been widely used in the literature (see for instance Brunet et al., 2017).

It is important to remark that this slide model can also be adapted to simulate subaerial landslides. The presence of the term $(1-r)$, in the definition of the Pouliquen-Folterre friction law, is due to the buoyancy effects, which must be taken
270   into account only in the case that the granular material layer is submerged in the fluid. Otherwise, this term must be replaced by (Brunet et al., 2017) in order to consider subaerial landslides.

In Macias et al. (2021) the reader can find the details about the numerical algorithms used to implement the model. The discretization of the resulting systems is difficult. For the hydrostatic systems that are expressed as non-conservative hyperbolic systems, the natural extension of the numerical schemes proposed in Escalante et al. (2018, 2019) has been
275   adopted, and then solved using a second order HLL (Harten-Lax-van Leer), positive-preserving, well-balanced, path-conservative finite-volume numerical scheme (see Castro and Fernandez-Nieto, 2012). Then, the non-hydrostatic pressure

corrections at the vertical interfaces required the discretization of an elliptic operator, and that was done using standard second-order central finite differences. This resulted in a linear system that was solved using an iterative scheduled

Jacobi method. Finally, the computed non-hydrostatic corrections were used to update the horizontal and vertical momentum equations at each layer, and, at the same time, the frictions were also discretized (see Escalante et al., 2018, 2019). For the discretization of the Coulomb friction term, the procedures presented in Fernández-Nieto et al. (2008) were followed.

The resulting 2D numerical scheme is well balanced for the water at rest stationary solution and is L^∞ stable under the normal CFL condition. The scheme is also positive preserving and can be used with emerging topographies.

For dealing with numerical experiments in 2D regions, the computational domain must be decomposed into cells, or finite volumes with a simple geometry. Here, a Cartesian type UTM was used. The 2D numerical algorithm for the hydrodynamic hyperbolic component of the coupled system is well suited to be parallelized and implemented in GPU architectures, as is shown in Castro et al (2011). Unfortunately, the standard treatment of the elliptic part of the system is not compatible with the parallelization of the algorithms. However, in Escalante et al. (2018, 2019), a multi-GPU implementation was presented and made possible because of the compactness of the numerical stencil, and the massive parallelization of the Jacobi method. Such a multi-GPU implementation of the complete algorithm results in much shorter computational times, and that is the reason why it was used in this work.

4 Results

4.1. The Storfjorden LS1 landslide geometry

The Storfjorden LS1 landslide is ~ 60 km in length and covers an area of more than 1300 km^2. Three main morphological elements are imaged by the multibeam bathymetry: headwall, sidewalls and sliding area (Fig. 3a). The headwall displays a well defined seaward-concave scarp that forms an amphiteatre-like feature about 8 km long and > 50 m in relief. Its slide scar is incised into the shelf-edge at 420-480 m water depth. The northwestern sidewall is defined by a striking 25 km long scarp, 35–40 m in relief, and with a rectilinear to slightly sinuous pathway. The southeastern 35 km long flank forms 25 to 80 m of relief, representing the highest in the middle domain (~1500 m water depth). The width between the sidewalls is variable downslope. The sidewalls are roughly parallel and define a bottle neck shape of 18 km wide, down at ~1330 m water depth, which increases to 32 km at ~1900 m water depth. The sliding area displays an elongated lobate shape, in plan-view, with an irregular seafloor. The seafloor gradients are typically 2º to 3º at ~1330 m water depth, and < 2º toward the distal ends, (Fig. 3b).

4.2. Submarine landslide and tsunami numerical simulations

310

The numerical simulation consists of several successive steps aimed at reconstructing: i) the smooth pre-landslide upper slope and landslide body geometry following the methods described in section 3.2.1 (Fig. 4), ii) the landslide dynamic, iii) the tsunami wave generation (Fig. 6) the tsunami wave propagation and its impacts on the coast (Figs. 7 and 8).

315 **4.2.1. Modeling the landslide dynamic**

Once the smooth pre-landslide upper slope had been calculated, following the methods described in section 3.2.1 (Fig. 4), the landslide body geometry was determined. The numerical landslide rupture simulation begins with the slope failure of the Storfjorden LS1, which assumes that it fails at once and moves downslope by gravitational forces (Macias et

320 al., 2016). Conventional studies about submarine slides show the difficulty in assessing whether their occurrence represents unique events. The morphological results would also support this assumption for the Storfjorden LS1, due to the lack of retrogressive structures, which would point to a decrease in the tsunamigenic potential (Harbitz et al 2006). In addition, by comparison with similar deposits from other continental slopes (Iglesias et al., 2012; Casas et al., 2013; Casas et al., 2017; Vanneste et al., 2006; Winkelmann et al., 2008), the Storfjorden LS1 shows a well-defined arcuate slide scar, mostly

325 rectilinear side walls, and a cutting basal shear surface. Its moving mass defines a subtabular body with chaotic deposits, and without apparent internal discontinuities that sharply interrupt the lateral continuity of the surrounding deposits (Pedrosa et al., 2011). All these characteristics put together tentatively point to a single process. The difference between pre-landslide and final bathymetry is 40 km^3, a volume that roughly matches the estimates proposed by Llopart et al. (2015). The numerical landslide rupture simulation shows that the moving mass was comprised of two domains with different behavior,

330 based on the velocity pattern (Figs. 3 and 4). An upper slope domain (Sl1-U, ~500 m water depth, ~3° slope gradients), which is related to the moving sediment nearest to the slide scar and moves faster with a v_p=67 m/s, and a slower middle slope domain (Sl1-M, ~1000 m water depth; 2° slope gradients) with a v_d=43 m/s, where the moving sediment shows the thickest values (70 m^3, Fig. 6, steps 1 to 2 and suppl. video 1). At ~1200 m water depth, the sliding velocities become homogeneous and slower, with a v_t=25 m/s at 25 min (Fig. 6, step 10 and suppl. video 1). This occurs when the faster

335 moving mass reaches the slower one. The landslide characteristics modeled by L-ML-HySEA determine an average velocity (v_a) of 21 m/s, a terminal time (t_t) of ~ 40 min, and a characteristic distance (d_c) of at least ~ 60 km.

340

345

Landslide geometry	V (km^3)	40
	X_1 Sl1-upper slope (m E)	490000
	Y_1 Sl1-upper slope (m N)	8350000
	X_2 Sl1-middle slope (m E)	485000
	Y_2 Sl1-middle slope (m N)	8340000
	h (m)	420
	l (km)	60
	w (km)	8
	T (km) base R1 to the top	0.375
	A_z (°)	N225°E
	Θ (°)	2°
Landslide dynamics	a_1 (m/s^2)	0.0113
	v_p (m/s)	67
	v_d (m/s)	43
	v_t (m/s)	25 m/s
	v_a (m/s)	21 m/s
	t_t (s)	~ 2400
	d_c (km)	~ 60
Initial tsunami	C_i (m)	0.3
	v_{ta} (m/s)	136
	v_r (m/s)	81
	v_n (m/s)	46.6
	v_e (m/s)	51.6

Table 1. Storfjorden SL1 geometry and mechanical characteristics. The inputs for the model are related to the landslide geometry: the total volume (V); the longitude and latitude of the submarine landslide relative to the Sl1-Upper slope area (X_1, Y_1), and in the Sl1-Mid slope area (X_2, Y_2); the initial depth (h) before the slope failure; the length (l) (long axis) and
350 width (w) (small axis); the maximum thickness (T); the mean azimuth direction of landslide (A_z); the mean slope gradient (Θ). The outputs of model are related to the landslide dynamic: the landslide initial acceleration (a_1); velocities to the landslide in the upper-slope (v_p) and the landslide located in the mid-slope (v_d); total velocity (v_t); average of velocity (v_a); its terminal duration (t_t); and characteristic distance (d_c). Initial crest (C_i) and average tsunami velocity at 1900 depth (v_{ta}), average velocity decrease during refraction (v_r), tsunami wave velocity toward northern (v_n), tsunami wave velocity toward
355 easthern (v_e).

4.2.2. Tsunami wave generation

360

Free water surface changes at any point along the time are determined according to seafloor deformation (Fig. 6 and suppl. video 1*)*. In the initial stage (4 to 5 min), the tsunami wave has two NW-SE trending dipoles, Sl1-U, smaller (25 km long) and more striking, and Sl1-M, larger (35 km long) and smoother. They have been created by the water-mass infilling the empty spaces produced by the sudden evacuations and uplifting of fast downslope moving mass. Both wave dipoles have
365 the troughs at shallower waters (~600 to 800 m) than their respective crests (~700 to 1000 m water depth) (Figs 6, step 1 and 7). The synthetic marigram on the upper slope (station 1) of the Storfjorden SL1 (Fig. 8a, b and c) highlights the initial wave generation with the crest and trough well-defined, registering a crest amplitude value of 0.4 m (above Sl1-U) and a trough amplitude value of up to -1.1 m at 3 min, followed by a crest amplitude value of 0.3 m (Figs. 7 step 1, 8b and suppl. video 2).

After 3 min, the two initial dipoles evolve into a single NW-SE trending dipole (crest amplitude value of 0.3 m),
370 whose trough (- 0.5 m) is, also at shallower waters (~1000 m) than the crest (~800 m) (Figs. 6 step 3, and 7 step 1). Wave rebound occurs (Fig. 6, step 4 to 9) when a maximum amplitude of ~2.7 m is registered over the distal area of the landslide (Fig. 8c, station 2, and suppl. video 2). At 7 to 9 minutes, a new crest wave amplitude value of 0.5 m appears parallel to the single dipole (Fig. 6, step 4 to 5 and suppl. video 1) at shallower waters (1400 m). It enlarges with time up to 0.7 m, whereas the trough largely keeps its dimensions or relief. At the 16 min mark, the tsunami wave reaches the highest amplitude, with a
375 trough amplitude value of -2 m and a crest amplitude value of 0.7 m (at 1780 m water depth).

At minute 25, the tsunami wave evolves into a larger dipole above the landslide, opposite to the first ones, with a trough amplitude value of -0.5 m and a crest amplitude value of 0.3 m (at 1200 m water depth). This dipole gets smaller with time, and a crest amplitude value of 0.5 m at shallower waters (900 m water depth) covering large areas with time (Fig. 6, step 10)

380 ### 4.2.3. Tsunami wave propagation and coastal impact

The tsunami wave dynamics are illustrated by the maps of the wave height across time (Fig. 7 and suppl. videos 1 and 2). Synthetic marigrams have been included at key locations in order to highlight the wave propagation and coastal impact in: the northwestern flank of Spitsbergen Bank (Fig. 8d, station 3); the onshore of Kveithola glacial trough (Fig. 8e, station 4);
385 the Spitsbergen Bank (Fig. 8f, station 5); the onshore northern boundary of mid-shelf of Storfjorden glacial trough (Fig. 8g, station 7); and the onshore southwestern Spitsbergen coast (Fig. 8h and i, stations 7 to 8).

The initial tsunami wave starts propagating from the landslide area with a trough wave moving northeast towards the coast, and a crest wave moving southwest (Fig. 7, step 3 and suppl. videos 1 and 2). The tsunami waves propagate
390 elliptically, with crest and trough elongated in the NW-SE direction (Fig. 6, step 3) at an average velocity (v_{ta}) of ~136 m/s. During the tsunami propagation from deep (1900 m) towards shallow water (250 m) (Fig. 7 and suppl. video 2), the refraction phenomenon occurs, (Fig. 8, station 3). This results in a wave front that shows a decrease in velocity (v_r= 81 m/s)
and an increase in amplitude. At station 4 (Fig. 8e), the values change from a trough amplitude of -0.25 m to a crest

amplitude value of 0.18 m. While at station 5, (Fig. 8f), the values change from a trough amplitude of -4.2 m to a crest

395 amplitude of 4.3 m. Furthermore, it can be observed that the tsunami propagation front displays a crescent shape.
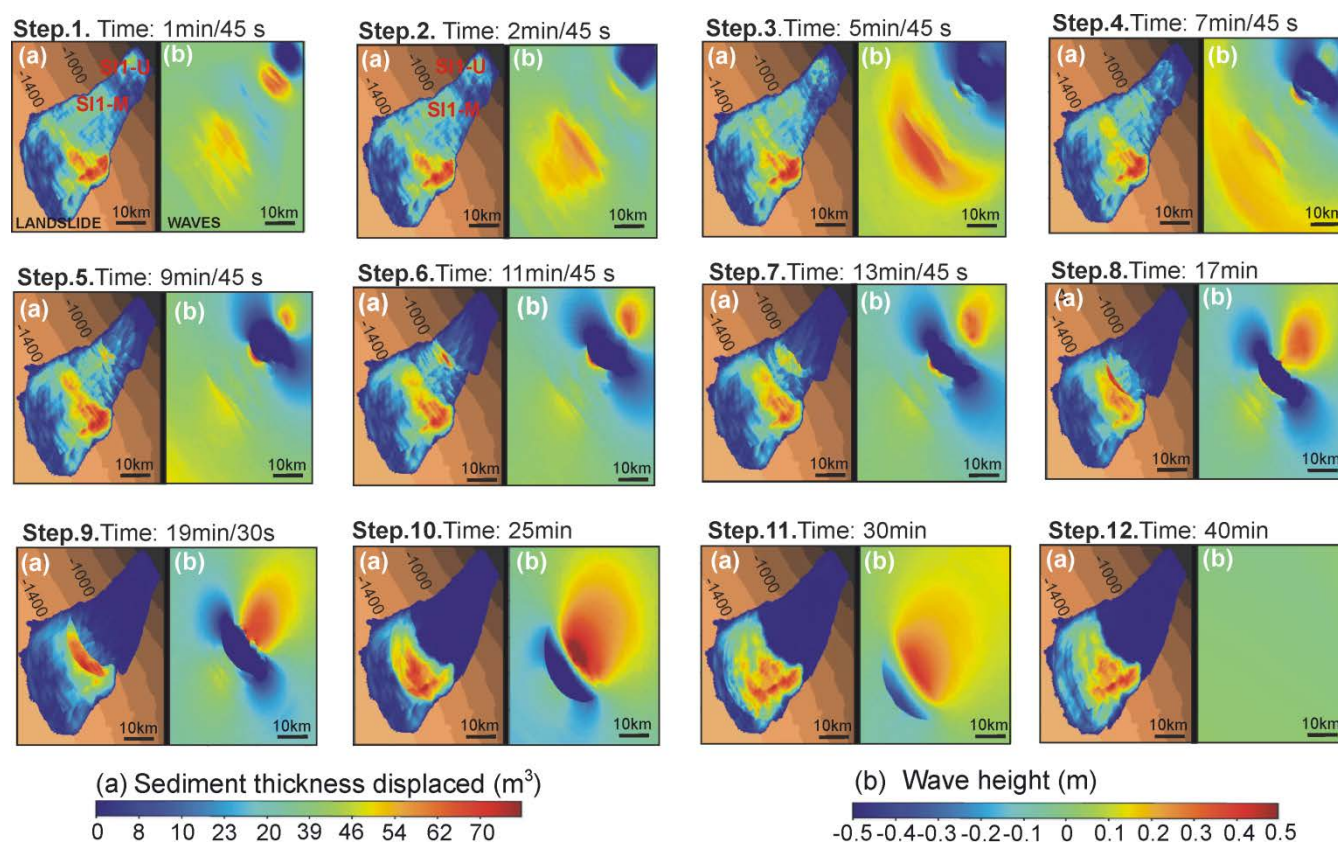
Figure 6. Main frame composition in twelve consecutive time-steps. (a) Evolution of the landslide. The color scale
corresponds with the sediment displaced, and the Sl1-U and SL1-M are the main sliding sectors. (b) Dipole waves evolution
of outgoing tsunami with the wavelength wave values.

Differences in tsunami arrival times are observed based on the propagation direction toward the coast. The tsunami

405 waves are slower moving toward the north and northeast (v_n= 46.6 m/s), than they are moving toward the east (v_e= 51.6 m/s)

(Fig. 7 and suppl. video. 2). Thus, the first impact of tsunami waves affects the Sørkappøya at 50 min (southern Spitsbergen),

with trough amplitude value of – 0.3 m, increasing to a crest amplitude value of 0.2 m at 75 min (Fig. 7 step 5 and 8h). The

second impact occurs at Kapp Dunnér (northwest Bear Island) with tsunami waves having a crest amplitude value of 0.3 m,

at 50 min, that increases to a crest amplitude value of 0.5 m at 53 min (Fig. 7 step 5 and suppl. video 2). After these two first

410 coastal impacts, the tsunami affects different parts of both islands at different times. The southwestern Bear Island is reached by the tsunami waves at 60 min with a maximum crest amplitude value of 0.5 m, (Fig. 7, step 6), followed by a trough amplitude value of -0.5 m at 65 min. Likewise, the north of Bear Island is affected by a trough amplitude value of -0.5 m (Fig. 7, step 6), withdrawal of the sea shoreline immediately before the tsunami waves arrives at 60 min, and a crest amplitude value of 0.5 m at 80 min (Fig. 7, step 7). In the Svalbard, the Stombukta Bay (southwestern Spitsbergen Island) is

415 the next impacted coastline (Fig. 8 a). There, the tsunami waves show specific velocity of v_s=13 m/s (at 18 m of depth), with trough amplitude values ~ -0.3 m at 63 min that increases crest amplitude value up to 0.32 m (85 to 95 min) (Fig 7 steps 7 to 8, and 8i). Finally, tsunami wave series propagating toward the coast occur until two hours after the Storfjorden SL1 landslide triggering.

420
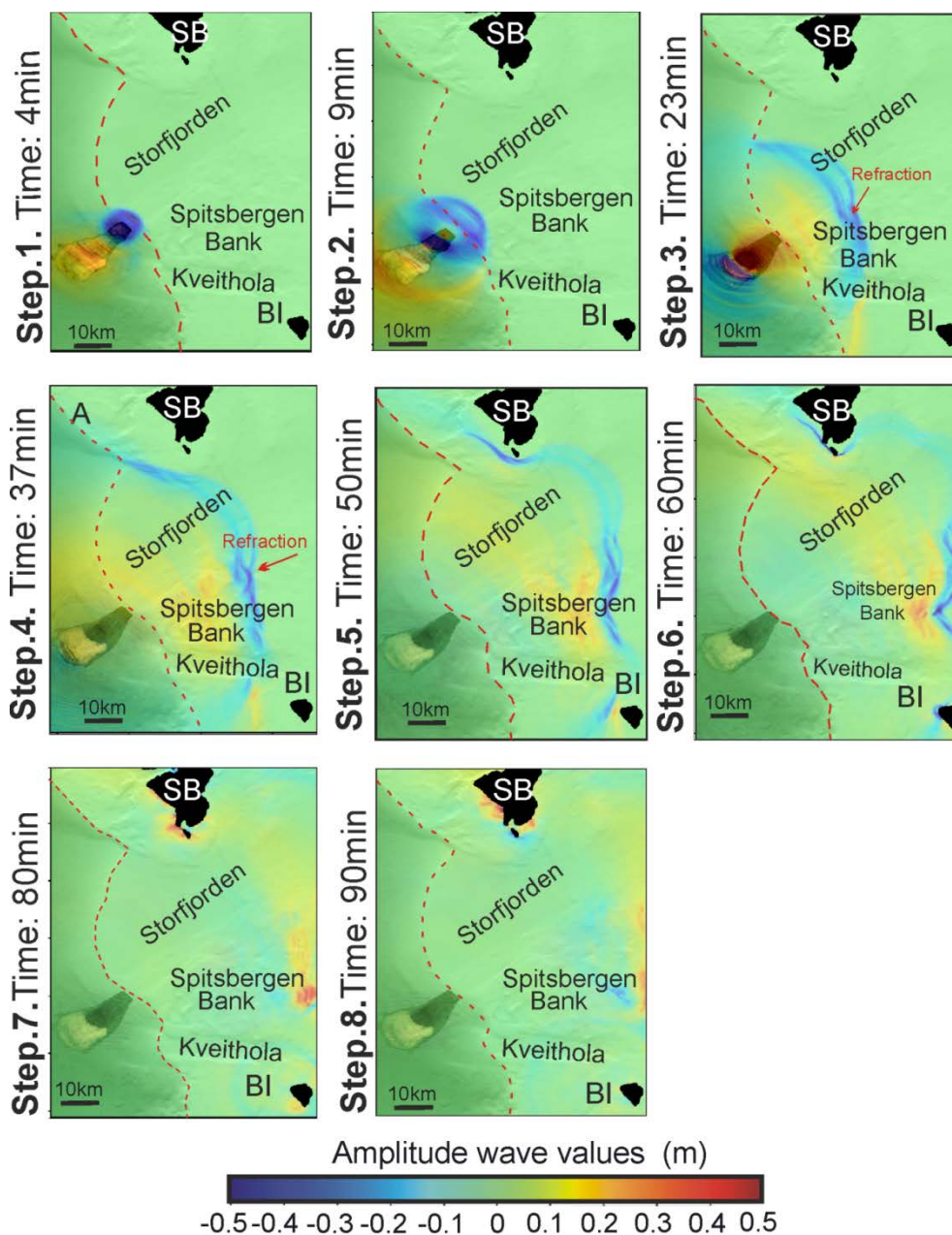
Figure 7. Seven steps that correspond with the tsunami waves generated at different times. The dotted red line indicates the
425 shelf break. The first step shows the generation of the tsunami wave and its spread. At 23 min the outgoing wave suffers
refraction. At 50 min the tsunami wave arrives at the northern coast of Bear Island. At 60 min, it hits the westernmost coast
of Spitsbergen.

5 Discussion and conclusions

430

The numerical simulation of Storfjorden SL1 landslide implemented by the L-ML-HySEA landslide tsunami model, which also includes the dispersion assessment (Macias et al., 2021), has confirmed it could trigger a tsunami. The tsunami waves would affect the nearby coast of the southwestern Spitsbergen (Svalbard) and Bear Island. Landslide (age, area, volume, seafloor gradients, location, and velocity) and related tsunami (wave amplitude, velocity) parameters of different landslide

435 inducing tsunamis have been compared with those defining the Storfjorden SL1 and its tsunami, in Table 2. The comparison indicates that the Storfjorden tsunami is consistent with the other tsunami parameters analyzed in the North Atlantic glaciated margin. Moreover, this study contributes to the literature with a new numerical model that explains the tsunamigenic potential of landslides, key for future predictions in the northern polar margins, at least. This is due to the potential occurrence, in the nearby future, of landslides related to global climate change and its related ocean warming

440 (Kattsov, et al., 2004; Berndt et al., 2009; Hanssen-Bauer et al., 2013; Skogseth, 2020). These interconnected facts are causing the rapid ice loss and glacier retreat that may influence (alone or in combination) the seafloor slope stability (Solheim et al., 2005; Berndt et al., 2009).
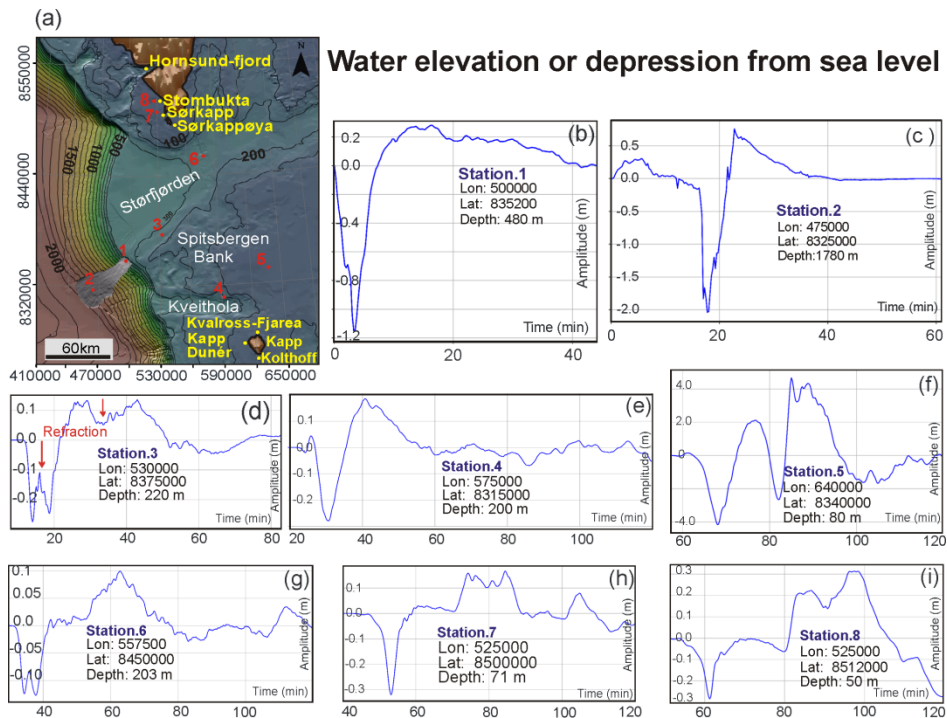
445

Figure 8. (a) The location map of the marigrams above the tsunami source (station.1 to 8). Note the different arrival times, periods, wave heights, and polarities at the different stations (b) to (i).

450   The L-ML-HySEA landslide tsunamigenic model provides a fast and consistent method for simulating landslide dynamics, tsunami wave generation, propagation and coastal impact. The results provide several fundamental insights regarding the assessment of the main factors that control the tsunami Storfjorden SL1 landslide characteristics and evolution, as well as the coastal hazard. They are the following:

455   **5.1. The landslide dynamics and wave generation**

Commonly, key landslide parameters for the generation of tsunamis include the volume, velocity and initial acceleration of the sliding mass (Harbitz et al., 2006; Urlaub et al., 2013; Løvholt et al., 2015; Úrgeles et al., 2018) (Table 1). In general, the total volume displaced conditions the size of the initial tsunami waves (Macias et al., 2015). The L-ML-HySEA model

460   indicates that the 40 km^3 of displaced volume of the Storfjorden SL1 landslide is enough to a trigger tsunami. By comparing this case with other landslide volumes in the surrounding areas (Fig, 1), this work highlights that not only large, but also relatively medium sized landslides, could have triggered tsunamis in the past. With respect to the initial acceleration, the velocity seems to be a key aspect for the development of impulsive events, such as translational slumps (Løvholt et al., 2015). We have tentatively suggested, above, that morphological results of the Storfjorden SL1 landslide point to an

465   impulsive slope failure event, and therefore, that velocity could play a remarkable role in our study case. In this sense, for the phase velocity to be highly effective at depths of H = 420 to 1900 m, during the tsunami waves onset, its value should be v_{ta}=136 m/s (Tinti and Bortolucci, 2000; Fryer et al., 2004). The relatively average velocity (roughly 21 m/s, Table 1) obtained for our tsunami indicates that it was out of phase, and therefore, it would not have been effective enough to create high amplitude tsunami waves (Huggel et al., 2005; Evans et al., 2009; Pudasaini., 2014; Dietrich and Krautblatter, 2019).

470

Our results indicate that the tsunami wave characteristics are influenced by landslide dynamics at two stages of the downslope moving mass: initial (4 to 5min) and late (25 min). The two initial wave dipoles, generated when seafloor failure occurs, are the consequence of two large seafloor depressions, one at the slide scar (i.e. main evacuation area), and the other one located between the two mass moving domains with different velocities. Their seafloor locations have conditioned water

475   depression at shallower waters than their respective water elevations. The different relative velocities may be due to the fact that the Storfjorden SL1 is moving over a palaeo-surface with uneven slope gradients that are higher (3º) where the mass moving velocity is faster (i.e. upper slope; v_p=67 m/s), and gentler (2º) where the velocity is slower (i.e. middle slope; v_d=43 m/s). The effects of seafloor gradients on landslide dynamics have been observed in other landslide analyses (Frey-Martínez et al., 2006; Moernaut and De Batist, 2011; Watt et al., 2012).

480

Event	Age (ky)	Area (km²)	Vol (km³)	Location	Wave amplitudes	Deposits type	Headwall depth (m) base slope (°)	Trigger	slide velocity (m/s)
Storfjorden SL1	< 200	1200	40	Storfjorden TMF	2.5 to 1	DF	420 to 1900 2° to 3°	A, B	25
Hinlopen	30	2400	1150	Arctic	130 to 40	HMW LRB TC	300 12° to 30º	A, B	-
Kongsfjorden TMF	-	9100	500 to 1000	Western Spitsbergen	1.5 to 5.6 (proximal) 0.6-1 (distal)	DF HMW	-	A, B	-
Bjornoyrenna	< 300	12500	1100	NW Barents	-	DF	400 2° to 3°	A, B	-
Gebra Valley	100	230	-	Central Bransfield Basin	-	DF	750 to 1930 2° to 1°	A, B	-
SFZS	130	230	4.5	-	-	-	1300 4.5° to 1°	-	-
Grand Banks	1929	20000	185	Newfoundland	3 to 8 (proximal) 9 to 15 (distal)	TC	500	B	-
Storegga	8.18	95000	2400 to 3200	North Atlantic	15	DF HMW	1000	B	-
Trænadjupet	4	-	900	Norway	0.3 to 1	DF HMW LRB	400	A, C	-
Nyk	16.3	2200	-	Norway	-	DF HMW	1200 to 1600	A, C	-
Skagway	1994	-	0.003	Alaska	13 to 7 (proximal) 1.3 to 0.2 (distal)	-	-	D	-
Lituya Bay	1598		0.31	Alaska	272 to 251 (proximal)	-	-	D	110
Big'95	11.5	2200	26	Western Mediterranean	8 to 6 (proximal) 4 to 2 (distal)	DF	200 to 1800	A, B	50

Table 2. Submarine landslides compared with Storfjorden SL1. V is the minimum volume of the landslide deposit and group refers to distinct depositional environments. Trigger: (A) Weaklayer Sedimentary Architecture, (B) Earthquake, (C) Gas Hydrate Dissociation, (D) Other additional factors. Deposits type: Huge mass wasting (HMW); large rafted blocks (LRB); turbidite currents (TC); debris flows (DF); slump blocks (SB). References: Storfjorden SL1 (Pedrosa et a., 2011; Lucchi et al., 2012; Rebesco et al., 2013; Llopart et al., 2015); Hinlopen (Winkelmann et al., 2008; Vanneste et al., 2006); Bjornoyrenna (Laberg et al., 1999); Gebra Valley (Garcia et al., 2008, Casas et al., 2013) Grand Banks (Piper et al., 1999; Fine et al., 2005); Storegga (Haflidason et al., 2004; Bondevik et al., 2012); Kongsfjorden TMF (Bernt et al., 2009);

Trænadjupet (Laberg et al., 2002b); Nyk (Lindberg and Laberg., 2004); Skagway (Thomson et al., 2001; Synolakis et al., 2002); Lituya-Bay (González-Vida et al., 2019); Big'95 (Iglesias et al., 2012).

495 At 25 min, a new dipole is formed, opposite to the previous ones. This new dipole is created when the faster sliding mass reaches the slower one, and both masses merge producing a significant impact in the thickness (50 m^3 to 70 m^3) of the distal moving mass. The increase in thickness would contribute to increase the pressure in the water column causing the uplift in the water surface and the enhancement of the tsunami waves (Ramadan et al., 2018; Ercilla et al., 2021).

500 Moreover, our study case points out that a proper understanding of landslide dynamics at their initial stages (or first motion), and of their deformation during the run-out, are crucial requirements for understanding the characteristics of the initial tsunami waves and the effects that those characteristics have on their evolution. In addition, our study case also suggests that identifying the initial tsunami wave forms could unveil the tsunami sources, e.g, landslides (generating single or multiple trough and crest pairs) *versus* faults (generating a single or crest wave) (e.g., Macias et al., 2016; Ercilla et al., 2021; Estrada et al., 2021; Bécel et al., 2017).

505

5.2. Seafloor morphology

It's widely known that how a tsunami wave propagates is highly dependent on the seafloor morphology (Urlaub 2013; Estrada et al., 2021). The model shows that tsunami waves propagate elliptically with respect to the NE-SW elongated 510 seafloor shape of the landslide relief. In the Storfjorden SL-1 tsunami, the average velocity waves (v_{ta}= 136 m/s) travel northeastern and are focused between the continental shelf of the Svalbard and of Bear Island, which helps to confine it and forces its direction of propagation (suppl. video 2). The continental shelf morphology determines tsunami shoaling, with the shallowest water depths at the Spitsbergen Bank (80 m water depth). The shoaling by the bank produces the refraction phenomenon and the amplification of the tsunami. As the tsunami propagates across the ocean, waves can undergo 515 refraction, which is caused by segments of the wave moving at different speeds as the water depth along the wave front varies (Berkhoff., 1972; Gangfeng, et al., 2012). Therefore, the refraction leads to an increase of the wave amplitude to a trough amplitude value of 4.2 and a crest amplitude value of 4.3 m (Fig. 7 station 5 and suppl. video 2), and a decrease in velocity (until v=81 m/s).

These shoaling effects have also been observed in other contexts, independently of the tsunami source (e.g., 520 Ioualalen, 2009; Shonting and Ezrailson, 2017). On the other hand, the crescent shapes of the tsunami front seem to be conditioned by the Storfjorden and Kveithola glacial troughs separated by the Spitsbergen Bank. The elongated negative reliefs of the glacial troughs would cause the funneling of the tsunami sea water with relative higher propagation specific velocities (v_s=56 m/s in Storfjorden glacial trough at 320 m water depth). The general shallow water depths of the continental shelf, and particularly the presence of the Spitsbergen Bank that represents an obstacle for the wave spreading,

525   induce a shoaling effect with wave refraction that decrease the amplitude of the tsunami waves (with trough amplitude value of -4.2 m) and the tsunami waves arrival, 15 min later at southwestern Spitsbergen, and 11 min later at northwestern Bear Island. When encountering an obstacle, the tsunami waves discharge their energy with great force, as in the case of Sørkappøya and Sørkapp at 75 min, with trough amplitude value of -0.5 m followed by crest amplitude value of 1.0 m, slowing down the arrival and amplitude of tsunami waves in the correlated bay at 100 min, with crest values between 0.2 m

530   and 0.4 m. The tsunami waves arrival is recorded at 80 to 95 min of at the eastern Hornsund-fjord, with trough amplitude value -0.3 m, followed by crest value 0.5 m. Therefore, the numerical simulations are a useful tool to assess tsunami hazard in places where local seafloor topography could amplify or delay the tsunami waves, and therefore the coastal impact.

5.3. Coastal location

535

The initial tsunami waves start propagating as negative and positive disturbance dipoles. The trough is always located towards the upper part of the margin, and generally determines that the first arrival to the coast corresponds to a sea level drop, hence decreasing the coastal impact. This, together with coastal location and orientation (i.e., angle of the waves with the coastline) condition the first arrival wave polarities to the coast, with negative amplitudes (-0.1 to -0.5 m) impacting in

540   the southwestern Spitsbergen, *versus* positive amplitude values (0.1 to 0.5 m) affecting the Bear Island (Fig. 7 and suppl. video 2). In the study area, the tsunami waves present low amplitude values at the coastal area and their arrival times are longer (50 to 80 min) than the tsunamis modeled in the nearby coast of western Spitsbergen (Bernt et al., 2009), where the slope failure is at shallower water depths (200 m) and the distance to the nearby coast is shorter (~ 90 km). Landslides triggered at shallower water result in more localized waves, and the elongated landslide velocity profile delays the

545   appearance of the first positive landward propagating wave, hence reducing the chances of constructive interference along the coast (Harbitz et al., 2006).

The submarine landslide geohazard studies are not an easy task due to the difficult access that the marine environment imposes for their accurate analysis and monitoring. This study case suggests that numerical modeling can help

550   to assist in the understanding of their dynamics and related tsunamigenic potentiality. A key point in the tsunamigenic landslide hazards assessment, in the northern high-latitude margins, is the probability of triggering "new" submarine landslides due to climatic warming stress on the ocean. The Storfjorden upper continental slope presents critical conditions to take into account, and warrants carrying out studies to assess slope-stability. Several factors support this assertion: (i) the overpressure ratios measured in the subsurface sediments (Lucchi et al., 2013; Llopart et al., 2019) and (ii) the seismicity

555   related with the active Horsund Fault Zone (Hampel et al., 2009; Auriac et al., 2016). In addition, this "new" environmental (iii) stress may intensify a process such as the gas-hydrate dissociation and fluid flow migration (León et al., 2021), and (iv) unloading rebound seismicity during ice retreat/melting (Berndt et al., 2009), which may contribute to trigger new submarine landslides.
560   In summary, our findings demonstrate that tsunami modelling induced by past landslides using the L-ML-HySEA landslide tsunami model, will be useful to provide new perspectives on tsunami hazard assessment in polar margins, where global climatic change and its related ocean warming may contribute to landslides trigger. Landslide tsunami models will allow us to identify the areas with maximum and faster coastal impact, and the effect of the local bathymetry in tsunami direction of propagation, shoaling, amplification and diffraction. This knowledge is very important for the design of early

565   warning strategies, as it will contribute to assess the key factors that would be useful as emergency planning tools.

Code availability.

The   source   code   of   SVAIS   and   EGLACOM   projects   used   in   this   study   is   available   from

570   https://sites.google.com/site/ipynicestreams/home

Data availability.

The L-ML-HySEA videos is aviable from https: //

575

Video Supplement

Video1: https://drive.google.com/file/d/17HrxTFjdA4ZUceWCbeMl_VNwat608D61/view?usp=sharing

Video2: https://drive.google.com/file/d/1vmjzn8HqgInSbycYXEMEgVy96gqbNFjn/view?usp=sharing

580

Author contributions

M.P., J.G. and G.E conceived the idea for the study and wrote the paper with methodological contributions from J.G.V. in

585   the tsunami mathematical model and S.O. and in the seafloor deformation and the tsunami potential. The geodynamic framework was done by M.T, J.G. and G.E. The compiled the seismic data and did the figures were done by M.T. The propagation tsunami model was done by J.G.V., S.O. and M.C. as well as associated videos. All authors provided guidance on the analyses and commented on the manuscript.

590   *Competing interests.*

The authors declare that they have no conflict of interest.

Acknowledgments.

595

This research was supported by Spanish IPY projects SVAIS (POL2006-07390/CGL) and IPY-NICE STREAMS (CTM2009-06370-E/ANT). Also the research group, RNM 148, and projects PAPEL B-RNM-301-UGR18 and AGORA P18-RT-3275 (Junta de Andalucía) and project GOLETA PID2019-108880RJ-I00 / AEI / 10.13039/501100011033. We would also like to thank the EDANYA research group from University of Malaga. Also all scientists and crew who participated in seagoing activities to obtain geophysical data in the framework of SVAIS cruise. We are grateful to Dag Ottesen (NGU) for providing the Norwegian Hydrographic Service Bathymetry. The authors wish to acknowledge the cooperation of Captain Pedro Luis de la Puente García-Ganges (*BIO Hespérides*), and of the technical staff at the UTM (CSIC, Barcelona). This work represents a contribution to CSIC Thematic Interdisciplinary Platform PTI POLARCSIC.

605 **References**

Auriac, A., Whitehouse, P. L., Bentley, M. J., Patton, H., Lloyd, J. M., and Hubbard, A: Glacial isostatic adjustment associated with the Barents Sea ice sheet: a modelling inter-comparison, Quat. Sci. Rev., 147, 122-135, doi:10.1016/j.quascirev.2016.02.011, 2016.

610 Bécel, A., Shillington, D. J., Delescluse, M., Nedimović, M. R., Abers, G. A., Saffer, D. M., and Kuehn, H: Tsunamigenic structures in a creeping section of the Alaska subduction zone, Nat. Geosci., 10(8), 609-613, doi: 10.1038/ngeo2990, 2017.

Bellwald, B., Hjelstuen, B. O., Sejrup, H. P., and Haflidason, H: Postglacial mass movements and depositional environments in a high-latitude fjord system–Hardangerfjorden, Western Norway, Mar. Geol., 379, 157-175, doi: 615 10.1016/j.margeo.2016.06.002, 2016.

Berkhoff, J.C.W: Computation of combined refraction-diffraction, in Coastal Engineering, 471-490, 1972.

Berndt, C., Brune, S., Nisbet, E., Zschau, J., and Sobolev, S. V: Tsunami modeling of a submarine landslide in the Fram Strait, Geochem. Geophys., 10 (4), doi:10.1029/2008GC002292, 2009.

Bondevik, S., Mangerud, J., Dawson, S., Dawson, and A., Lohne, Ø: Record-breaking height for 8000-year-old tsunami in 620 the North Atlantic, EOS, 84 (31), 289-297, doi: 10.1029/2003EO310001, 2003.

Bondevik, S., Stormo, S. K., and Skjerdal, G: Green mosses date the Storegga tsunami to the chilliest decades of the 8.2 ka cold event, Quat. Sci. Rev., 45, 1-6, doi:10.1016/j.quascirev.2012.04.020, 2012.

Brunet, M., Moretti, L., Le Friant, A., Mangeney, A., Fern´andez Nieto, E.D., and Bouchut, F: Numerical simulation of the 30–45 ka debris avalanche flow of Montagne Pelée volcano, Martinique: from volcano flank collapse to submarine 625 emplacement, Nat. Hazards, 87, 1189–1222, doi: 10.1007/s11069-017-2815-5, 2017.

Bryn, P., Berg, K., Forsberg, C. F., Solheim, A., and Kvalstad, T. J: Explaining the Storegga Slide Mar. Pet. Geol.,22(1-2), 11-19, doi:10.1016/B978-0-08-044694-3.50005-6, 2005.

Bugge, T., Befring, S., Belderson, R.H., Eidvin, T., Jansen, E., Kenyon, N., Holtedahl, H., and H.P.Sejrup: A giant three-stage submarine slide off Norway, Geo-Marine Letters, 7, 191–198, 1987.

630   Butt, F.A., Elverhøi, A., Solheim, A., and Forsberg, C.F: Deciphering late Cenozoic development of the western Svalbard Margin from ODP Site 986 results, Mar. Geol 169 (3-4), 373–390, doi:10.1016/S0025-3227(00)00088-8, 2000.

Canals, M., Lastras, G., Urgeles, R., Casamor, J. L., Mienert, J., Cattaneo, A., De Batist, M., Haflidason, H., Imbo, Y., Laberg, J. S., Locat, J., Long, D., Longva, O., Masson, D. G., Sultan, N., Trincardi, F., and Bryn, P: Slope failure dynamics and impacts from seafloor and shallow sub-seafloor geophysical data: case studies from the COSTA project,
635   Mar. Geol., 213(1-4), 9–72, doi: 10.1016/j.margeo.2004.10.001, 2004.

Casas, D., Ercilla, G., García, M., Yenes, M., and Estrada, F: Post-rift sedimentary evolution of the Gebra Debris Valley. A submarine slope failure system in the Central Bransfield Basin (Antarctica), Mar Geol, 340, 16-29, doi: 10.1016/j.margeo.2013.04.011, 2013.

Castro Díaz, M. J., and Fernández-Nieto, E: A class of computationally fast first order finite volume solvers: PVM methods,
640   SIAM, J.Sci. Comput., 34(4), A2173-A2196, doi: 10.1137/100795280, 2012.

Castro, M. J., Ortega, S., De la Asuncion, M., Mantas, J. M., and Gallardo, J. M: GPU computing for shallow water flow simulation based on finite volume schemes, C. R. Mec., 339(2-3), 165-184, doi: 10.1016/j.crme.2010.12.004, 2011.

Chiocci, F. L., and Ridente, D: Regional-scale seafloor mapping and geohazard assessment. The experience from the Italian project MaGIC (Marine Geohazards along the Italian Coasts), Mar. Geophys. Res., 32(1), 13-23, doi: 10.1007/s11001-
645   011-9120-6, 2011.

Dietrich, A., and Krautblatter, M: Deciphering controls for debris-flow erosion derived from a LiDAR-recorded extreme event and a calibrated numerical model, Earth Surf. Process. Landf, 44(6), 1346-1361, doi: doi.org/10.1002/esp.4578, 2019.

Eck, M., and Hoppe, H: Automatic reconstruction of B-spline surfaces of arbitrary topological type, In Proceedings of the
650   23rd annual conference on Computer Graphics and Interactive Techniques, 325-334, 1996.

Eiken, O: Seismic Atlas of Western Svalbard, Norsk Polarinstitutts Meddelelser, 130, 73, ISBN, 82-7666-067-3, 1994.

Elverhøi, A., de Blasio, A., Butt, F.A., Issler, F.A., Harbitz, d., Engvik, L., Solheim, A., and Marr, J: Submarine mass-wasting on glacially-influenced continental slopes: processes and dynamics, J. Geol Soc London, 203, 73-87, doi:10.1144/GSL.SP.2002.203.01.05, 2002.

655   Engen, Ø., Faleide, J. I., and Dyreng, T. K: Opening of the Fram Strait gateway: A review of plate tectonic constraints, Tectonophysics, 450 (1), 51–69, doi: 10.1016/j.tecto.2008.01.002, 2008.

Ercilla, G., Casas, D., Alonso, B., Casalbore, D., Estrada, F., Idárraga-García, J., López-González, N., Pedrosa, M., Teixeira, M., Sánchez-Guillamón, O., Azpiroz-Zabala, M., Bárcenas, P., Chiocci, F. L., García, M., Galindo-Zaldívar, J., Geyer,

A., Gómez-Ballesteros, M., Juan, C., Martorelli, and E.,Yenes, M: Deep Sea Sedimentation (J. (Jack) F. B. T.T. on G.
660   (Second E. Shroder (ed.); (960–988), 2022, Academic Press, doi:10.1016/B978-0-12-818234-5.00129-2, 2022.

Escalante, C., Morales de Luna, T., and Castro, M. J: Non-hydrostatic pressure shallow flows: GPU implementation using
       finite volume and finite difference scheme, Applied Mathematics and Computation, 338, 631-659, doi:
       10.1016/j.amc.2018.06.035, 2018.

Escalante, C., Dumbser, M., and Castro, M. J: An efficient hyperbolic relaxation system for dispersive non-hydrostatic water
665   waves and its solution with high order discontinuous Galerkin schemes, Journal of Computational Physics, 394, 385-416,
       doi: 10.1016/j.jcp.2019.05.035, 2019.

Estrada, F., González-Vida, J. M., Peláez, J. A., Galindo-Zaldívar, J., Ortega, S., Macías, J., and Ercilla, G: Tsunami
       generation potential of a strike-slip fault tip in the westernmost Mediterranean, Sci. Rep. 11(1), 1-9, doi: 10.1038/s41598-
       021-95729-6, 2021.

670   Faleide, J. I., Vågnes, E., and Gudlaugsson, S. T: Late Mesozoic–Cenozoic evolution of the southwestern Barents Sea in a
       regional rift-shear tectonic setting, Mat. Pet. Geol., 10(3), 186-214, doi: 10.1016/0264-8172(93)90104-Z, 1993.

Faleide, J.I., Tsikalas, F., Breivik, A.J., Mjelde, R., Ritzmann, O., Wilson, J., and Eldholm, O: Structure and evolution of the
       continental margin off Norway and the Barents Sea, 31, 82–91, doi: 10.18814/epiiugs/2008/v31i1/012 , 2008.

Fernandez-Nieto, E., Parisot, M., Penel, Y., and Sainte-Marie, J: A hierarchy of dispersive layer-averaged approximations of
675   Euler equations for free surface flows, Communications in Mathematical Sciences 16, 1169–1202, 2018.

Fernández-Nieto, E.D., Bouchut, F., Bresch, D. Castro., and M.J., Mangeney, A: A new Savage–Hutter type model for
       submarine avalanches and generated tsunami, J. Comput. Phys, 227, 7720-775, doi: 10.1016/j.jcp.2008.04.039, 2008.

Fiedler, A. and Faleide, J.I: Cenozoic sedimentation along the southwestern Barents Sea margin in relation to uplift and
       erosion of the shelf, Glob. Planet. Change.,12, 75–93, doi: 10.1016/0921-8181(95)00013-5, 1996.

680   Fine, I. V., Rabinovich, A. B., Bornhold, B. D., Thomson, R. E., and Kulikov, E. A: The Grand Banks landslide-generated
       tsunami of November 18, 1929: preliminary analysis and numerical modeling, Mar. Geol., 215(1-2), 45-57, doi:
       10.1016/j.margeo.2004.11.007, 2005.

Førland, E. J., Jacobsen, J. K. S., Denstadli, J. M., Lohmann, M., Hanssen-Bauer, I., Hygen, H. O., and Tømmervik, H: Cool
       weather tourism under global warming: Comparing Arctic summer tourists' weather preferences with regional climate
685   statistics and projections, Tourism Management, 36, 567-579, doi:10.1016/j.tourman.2012.09.002, 2013.

Frey-Martínez, J., Cartwright, J., and James, D: Frontally confined versus frontally emergent submarine landslides: A 3D
       seismic characterization, Mar. Pet. Geol., 23(5), 585-604, doi:10.1016/j.marpetgeo.2006.04.002, 2006.

Fryer, G. J., Watts, P., and Pratson, L. F: Source of the great tsunami of 1 April 1946: a landslide in the upper Aleutian
       forearc, Mar. Geol., 203(3-4), 201-218, doi: 10.1016/S0025-3227(03)00305-0, 2004.

690   García, M., Ercilla, G., and Alonso, B. Morphology and sedimentary systems in the Central Bransfield Basin, Antarctic
       Peninsula: sedimentary dynamics from shelf to basin, Basin. Res., 21(3), 295-314, doi: 10.1111/j.1365-
       2117.2008.00386.x, 2009.

García, M., Ercilla, G., Alonso, B., Casas, D., and Dowdeswell, J. A: Sediment lithofacies, processes and sedimentary models in the Central Bransfield Basin, Antarctic Peninsula, since the Last Glacial Maximum, Mar. Geol., 290(1), 1–16,
695   doi: 10.1016/j.margeo.2011.10.006, 2011.

González-Vida, J. M., Macías, J., Castro, M. J., Sánchez-Linares, C., de la Asunción, M., Ortega-Acosta, S., and Arcas, D: The Lituya Bay landslide-generated mega-tsunami–numerical simulation and sensitivity analysis, Natural Hazards and Earth System Sciences, 19(2), 369-388, doi: 10.5194/nhess-19-369-2019, 2019.

Haflidason, H., Sejrup, H. P., Nygård, A., Mienert, J., Bryn, P., Lien, R., and Masson, D: The Storegga Slide: architecture,
700   geometry and slide development, Marine geology, 213(1-4), 201-234, doi: 10.1016/j.margeo.2004.10.007, 2004.

Haflidason, H., Lien, R., Sejrup, H. P., Forsberg, C. F., and Bryn, P: The dating and morphometry of the Storegga Slide, Mar.Pet. Geol., 22 (1), 123–136, doi:10.1016/j.marpetgeo.2004.10.008, 2005.

Hampel, A., Hetzel, R., Maniatis, G., and Karow, T: Three-dimensional numerical modeling of slip rate variations on normal and thrust fault arrays during ice cap growth and melting, J. Geophys. Res., 114 (B8) 406, doi: 10.1029/2008JB006113,
705   2009.

Harbitz, C. B., Løvholt, F., Pedersen, G., and Masson, D. G: Mechanisms of tsunami generation by submarine landslides: a short review, N. J. Geol, 86(3), 2006.

Huggel, C., Zgraggen-Oswald, S., Haeberli, W., Kääb, A., Polkvoj, A., Galushkin, I., and Evans, S. G: The 2002 rock/ice avalanche at Kolka/Karmadon, Russian Caucasus: assessment of extraordinary avalanche formation and mobility, and
710   application of QuickBird satellite imagery, Nat. Hazards Earth Syst. Sci, 5(2), 173-187, doi: 10.5194/nhess-5-173-2005, 2005.

Iglesias, O., Lastras, G., Canals, M., Olabarrieta, M., Gonzalez, M., Aniel-Quiroga, Í., and De Mol, B: The BIG'95 submarine landslide–generated tsunami: a numerical simulation, The Journal of Geology, 120(1), 31-48, doi: 10.1086/662718, 2012.

715 Imamura, F., Boret, S. P., Suppasri, A., and Muhari, A: Recent occurrences of serious tsunami damage and the future challenges of tsunami disaster risk reduction, Progress in Disaster Science, 1, 100009, doi: 10.1016/j.pdisas.2019.100009, 2019.

Innocenti, C., Battaglini, L., D'Angelo, S., and Fiorentino, A: Submarine landslides: mapping the susceptibility in European seas, Q. J. Eng. Geol. Hydrogeol., 54(1), doi:10.1144/qjegh2020-027, 2021.

720 Ioualalen, M., Rentería, W., Ilayaraja, K., Chlieh, M., Arreaga-Vargas, P: A synoptic picture of the impact of the 26th December 2004 Indian Ocean tsunami on the coast of Sri Lanka, Environmental modelling software, 25(12), 1874-1880, doi: 10.1016/j.envsoft.2010.04.010, 2010.

Knies, J., Matthiessen, J., Vogt, C., Laberg, J.S., Hjelstuen, B.O., Smelror, M., Larsen, E., Andreassen, K., Eidvin, T., Vorren, T.O: The Plio-Pleistocene glaciation of the Barents Sea–Svalbard region: a new model based on revised
725   chronostratigraphy, Quat. Sci. Rev., 28, 812–829, doi:10.1016/j.quascirev.2008.12.002, 2009.

Kvalstad, T. J., Andresen, L., Forsberg, C. F., Berg, K., Bryn, P., and Wangen, M: The Storegga slide: evaluation of triggering sources and slide mechanics,Editor(s): Solheim, A., Bryn, P., Berg, K., Sejrup., H.PMIENERT., J, Ormen Lange–an Integrated Study for Safe Field Development in the Storegga Submarine Area, Elsevier, 245–256, doi: 10.1016/B978-0-08-044694-3.50025-1, 2005.

730 L'Heureux, J.S., Vanneste, M., Rise, L., Brendryen, J., Forsberg, C.F., Nadim, F., Longva, O., Chand, S., Kvalstad, T.J., and Haflidason, H: Stability, mobility and failure mechanism for landslides at the upper continental slope off Vesterålen, Norway, Mar. Geol. 346, 192–207, doi:10.1016/j.margeo.2013.09.009, 2013.

Laberg, J.S., Vorren, T.O., Dowdeswell, J.A., Kenyon, N.H., and Taylor, J: The Andøya Slide and the Andøya Canyon, north-eastern Norwegian–Greenland Sea, Mar Geol, 162(2-4), 259-275, 2000.

735 Laberg, J.S., and Vorren, T.O: A Late Pleistocene submarine slide on the Bear Island Trough Mouth Fan, Geo-Mar. Lett., 13, 227–234, doi:10.1007/BF01207752, 1993.

Lee, H. J: Timing of occurrence of large submarine landslides on the Atlantic Ocean margin, Mar. Geol., 264(1–2), 53–64, doi: 10.1016/j.margeo.2008.09.009, 2009.

Lee, S., Wolberg, G., and Shin, S. Y: Scattered data interpolation with multilevel B-splines, IEEE transactions on 740 visualization and computer graphics, 3(3), 228-244, doi: 10.1109/2945.620490, 1997.

León, R., Llorente, M., and Giménez-Moreno, C. J: Marine Gas Hydrate Geohazard Assessment on the European Continental Margins. The Impact of Critical Knowledge Gaps, Appl. Sci., 11(6), 2865, doi: 10.3390/app11062865, 2021.

Lindberg, B., Laberg, J. S., and Vorren, T. O: The Nyk Slide—morphology, progression, and age of a partly buried submarine slide offshore northern Norway, Mar. Geol., 213(1-4), 277-289, doi: 10.1016/j.margeo.2004.10.010, 2004.

745 Llopart, J. Storfjorden Trough Mouth Fan (Western Barents Sea): Slope Failures in Polar Continental Margins; Significance of Stress Changes and Fluid Migration Induced by Glacial Cycles, PhD thesis, Universitat de Barcelona, pp. 231, http://hdl.handle.net/2445/108581, 2016.

Llopart, J., Urgeles, R., Camerlenghi, A., Lucchi, R.G., Rebesco, M., and De Mol, B: Late Quaternary development of the Storfjorden and Kveithola Trough Mouth Fans, northwestern Barents Sea, Quat. Sci. Rev. 129, 68–84, 2012, doi: 750 10.1016/j. quascirev.2015.10.002, 2015.

Llopart, J., Urgeles, R., Forsberg, C. F., Camerlenghi, A., Vanneste, M., Rebesco, M., and Lantzsch, H: Fluid flow and pore pressure development throughout the evolution of a trough mouth fan, western Barents Sea, Basin Research, 31(3), 487-513, doi:10.1111/bre.12331, 2019.

Løvholt, F., Glimsdal, S., and Harbitz, C. B: On the landslide tsunami uncertainty and hazard, Landslides, 17(10), 2301-755 2315, doi: 10.1007/s10346-020-01429-z, 2020.

Løvholt, F., Pedersen, G., Harbitz, C. B., Glimsdal, S., and Kim, J: On the characteristics of landslide tsunamis, Phil. Trans. R. Soc. A.3732014037620140376, doi:10.1098/rsta.2014.0376, 2015.

Lucchi, R. G., Camerlenghi, A., Rebesco, M., Colmenero-Hidalgo, E., Sierro, F. J., Sagnotti, L., and Caburlotto, A: Postglacial sedimentary processes on the Storfjorden and Kveithola trough mouth fans: Significance of extreme glacimarine sedimentation, Glob. Planet. Change, 111, 309-326, doi:10.1016/j.gloplacha.2013.10.008, 2013.

Lucchi, R.G., Pedrosa, M.T., Camerlenghi, A., Urgeles, R., De Mol, B., and Rebesco, M: Recent submarine landslides on the continental slope of Storfjorden and Kveithola Trough-Mouth Fans (North West Barents Sea). In: Yamada, Y., Kawamura, K., Ikehara, K., Ogawa, Y., Urgeles, R., Mosher, D., Chaytor, J., Strasser, M. (Eds.), Submarine Mass Movement and Their Consequences, Advances in Natural and Technological Hazards Research. 31. Springer, Dordrecht (The Netherlands), pp. 735–745, 2012, doi: 10.1007/978-94-007-2162-3_65, 2012.

Macías, J., Vázquez, J. T., Fernández-Salas, L. M., González-Vida, J. M., Bárcenas, P., Castro, M. J., Díaz-del-Río, V., and Alonso, B: The Al-Borani submarine landslide and associated tsunami, A modelling approach, Mar. Geol, 361, 79–95, doi: 10.1016/j.margeo.2014.12.006, 2015.

Maslin, M., Mikkelsen, N., Vilela, C., and Haq, B: Sea-level–and gas-hydrate–controlled catastrophic sediment failures of the Amazon Fan, Geology, 26(12), 1107-1110, doi: 10.1130/0091-7613(1998)026<1107:SLAGHC>2.3.CO;2, 1998.

Meleshko, V. P., Golitsyn, G. S., Govorkova, V. A., Demchenko, P. F., Eliseev, A. V., Kattsov, V. M., and Sporyshev, P. V: Anthropogenic climate change in Russia in the 21st century: An ensemble of climate model projections, Meteorologiya i gidrologiya, 4, 38-49, 2004.

Moernaut, J., and De Batist, M: Frontal emplacement and mobility of sublacustrine landslides: results from morphometric and seismostratigraphic analysis, Mar. Geol, 285(1-4), 29-45, doi: 10.1016/j.margeo.2011.05.001, 2011.

Moernaut, J., Van Daele, M., Strasser, M., Clare, M. A., Heirman, K., Viel, M., Cardenas, J., Kilian, R., Ladrón de Guevara, B., Pino, M., Urrutia, R.,and De Batist, M: Lacustrine turbidites produced by surficial slope sediment remobilization: A mechanism for continuous and sensitive turbidite paleoseismic records, Mar. Geol, 384, 159-176. doi:10.1016/j.margeo.2015.10.009, 2017.

Newton, A. M., and Huuse, M: Glacial geomorphology of the central Barents Sea: implications for the dynamic deglaciation of the Barents Sea Ice Sheet, Mar. Geol, 387, 114-131, doi:10.1016/j.margeo.2017.04.001, 2017.

Ottesen, D., Dowdeswell, J.A., and Rise, S: Submarine landforms and the reconstruction of fast-flowing ice streams within a large Quaternary ice sheet: The 2500-km- long Norwegian-Svalbard margin (57°–80°N), Geol. Soc. Am. Bull., 117, 1033–1050, doi: doi.org/10.1130/B25577.1, 2005.

Pedrosa, M. T., Camerlenghi, A., De Mol, B., Urgeles, R., Rebesco, M., and Lucchi, R. G: Seabed morphology and shallow sedimentary structure of the Storfjorden and Kveithola trough-mouth fans (North West Barents Sea), Mar. Geol, 286(1-4), 65-81, doi: 10.1016/j.margeo.2011.05.009, 2011.

Piper, D. J., Cochonat, P., and Morrison, M. L: The sequence of events around the epicentre of the 1929 Grand Banks earthquake: initiation of debris flows and turbidity current inferred from sidescan sonar, Sedimentology, 46(1), 79-97, doi: 10.1046/j.1365-3091.1999.00204.x, 1999.

Pirli, M., Schweitzer, J., and Paulsen, B: The Storfjorden, Svalbard, 2008–2012 aftershock sequence: Seismotectonics in a polar environment, Tectonophysics, 601, 192–205. doi:10.1016/j.tecto.2013.05.010, 2013.

Pouliquen, O., and Forterre, Y: Friction law for dense granular flows: application to the motion of a mass down a rough inclined plane, Journal of fluid mechanics, 453, 133-151, doi: 10.1017/S0022112001006796, 2002.

795   Pudasaini, S. P: Dynamics of submarine debris flow and tsunami, Acta Mechanica, 225(8), 2423-2434, doi: 10.1007/s00707-014-1126-0, 2014.

Ramadan, K.T: Near- and far-field tsunami waves, displaced water volume, potential energy and velocity flow rates by a stochastic submarine earthquake source model, Nat. Hazards Earth Syst. Sci. Discuss, doi: 10.5194/nhess-2018-107, 2018.

800   Rebesco, M., Laberg, J. S., Pedrosa, M. T., Camerlenghi, A., Lucchi, R. G., Zgur, F., and Wardell, N: Onset and growth of Trough-Mouth Fans on the North-Western Barents Sea margin -implications for the evolution of the Barents Sea/Svalbard Ice Sheet, Quat. Sci. Rev., 92, 227–234, doi:10.1016/j.quascirev.2013.08.015, 2013.

Rebesco, M., Pedrosa, M.T., Camerlenghi, A., Lucchi, R.G., Sauli, C., De Mol, B., Madrussani, G., Urgeles, R., Rossi, G., and Böhm, G: One million years of climatic generated landslide events on the northwestern Barents Sea continental

805   margin. In: Yamada, Y., Kawamura, K., Ikehara, K., Ogawa, Y., Urgeles, R., Mosher, D., Chaytor, J., Strasser, M. (Eds.), Submarine Mass Movements and Their Consequences. Advances in Natural and Technological Hazards Research. 31, Springer, Dordrecht (The Netherlands), pp. 747–756, doi: 10.1007/978-94-007-2162-3-66, 2012.

Rodríguez-Morata, C., Villacorta, S., Stoffel, M., and Ballesteros-Cánovas, J. A: Assessing strategies to mitigate debris-flow risk in Abancay province, south-central Peruvian Andes, Geomorphology, 342, 127–139,

810   doi:10.1016/j.geomorph.2019.06.012, 2019.

Shonting, D., and Ezrailson, C: The Chicxulub Tsunami, In: Chicxulub: The Impact and Tsunami, Springer, Praxis, Book, Cham, 69-106, doi: 10.1007/978-3-319-39487-9_4, 2017.

Sierro, F. J., Andersen, N., Bassetti, M. A., Berné, S., Canals, M., Curtis, J. H., Dennielou, B., Flores, J. A., Frigola, J., Gonzalez-Mora, B., Grimalt, J. O., Hodell, D. A., Jouet, G., Pérez-Folgado, M., and Schneider, R: Phase relationship

815   between sea level and abrupt climate change, Quat. Sci. Rev., 28(25), 2867–2881, doi: 10.1016/j.quascirev.2009.07.019, 2009.

Skogseth, R., Olivier, L. L., Nilsen, F., Falck, E., Fraser, N., Tverberg, V., and Falk-Petersen, S: Variability and decadal trends in the Isfjorden (Svalbard) ocean climate and circulation–An indicator for climate change in the European Arctic, Prog. Oceanogr., 187, 102394, doi:10.1016/j.pocean.2020.102394, 2020.

820   Solheim, A., Berg, K., Forsberg, C. F., and Bryn, P: The Storegga Slide complex: repetitive large scale sliding with similar cause and development, Marine and Petroleum Geology, 22(1-2), 97-107, doi.org:10.1016/j.marpetgeo.2004.10.013, 2004.

Sun, Q., and Leslie, S: Tsunamigenic potential of an incipient submarine slope failure in the northern South China Sea, Mar. Pet. Geol., 112, 104111. doi: 10.1016/j.marpetgeo.2019.104111, 2020.

825   Synolakis, C. E., Yalciner, A. C., Borrero, J. C., and Plafker, G: Modeling of the November 3, 1994 Skagway, Alaska tsunami, In Solutions to Coastal Disasters, 915-927, 2002.

Talling, P. J: On the triggers, resulting flow types and frequencies of subaqueous sediment density flows in different settings: Mar. Geol., 352, 155-182, doi:10.1016/j.margeo.2014.02.006, 2014.

Tappin, D. R: Submarine mass failures as tsunami sources: their climate control, Phil. Trans. R. Soc. A, 368(1919), 2417-2434, doi:10.1098/rsta.2010.0079, 2010.

830

Thomson, R. E., Rabinovich, A. B., Kulikov, E. A., Fine, I. V., and Bornhold, B. D: On numerical simulation of the landslide-generated tsunami of November 3, 1994 in Skagway Harbor, Alaska. In Tsunami research at the end of a critical decade, 243-282, Springer, Dordrecht, doi: 10.1007/978-94-017-3618-3_17, 2001.

Tinti, S., Bortolucci, E., and Romagnoli, C: Computer simulations of tsunamis due to sector collapse at Stromboli, Italy, Journal of Volcanology and Geothermal Research, 96(1-2), 103-128, doi: 10.1016/S0377-0273(99)00138-9, 2000.

835

Urgeles, R., Bahk, J. J., Lee, S. H., Horozal, S., Cukur, D., Kim, S. P, Kim, J.Y., S.W, Jeong., I.K., U: Tsunami hazard from submarine landslides: scenario-based assessment in the Ulleung Basin, East Sea (Japan Sea), Geoscience Journal, 23, 439–460, doi: 10.1007/s12303-018-0044-x, 2019.

Urlaub, M., Talling, P.J., and Masson, D.G: Timing and frequency of large submarine landslides: implications for

840   understanding triggers and future geohazard, Quat. Sci. Rev., 72, 63–82, doi:10.1016/j.quascirev.2013.04.020, 2013.

Vanneste, M., Mienert, J., and Bünz, S: The Hinlopen Slide: a giant, submarine slope failure on the northern Svalbard margin, Arctic Ocean, EARTH & PLANET. SCI. LETT., 245(1-2), 373-388, doi: 10.1016/j.epsl.2006.02.045, 2006,

Vanneste, M., Harbitz, C. B., De Blasio, F. V., Glimsdal, S., Mienert, J., and Elverhøi, A: Hinlopen-Yermak Landslide, Arctic Ocean Geomorphology, landslide dynamics and tsunami simulations, Mass-Transport Deposits (in) Deepwater

845   Settings, edited by: Shipp, R., Weimer, P., and Posamentier, H, 96, 2011.

Vanneste, M., Sultan, N., Garziglia, S., Forsberg, C. F., and L'Heureux, J. S: Seafloor instabilities and sediment deformation processes: The need for integrated, multi-disciplinary investigations, Mar. Geol., 352, 183-214, doi: 10.1016/j.margeo.2014.01.005, 2014.

Waddington, C., and Wicks, K: Resilience or wipe out? Evaluating the convergent impacts of the 8.2 ka event and Storegga

850   tsunami on the Mesolithic of northeast Britain, J. Archaeol. Sci. Rep, 14, 692-714, doi: 10.1016/j.jasrep.2017.04.015, 2017.

Watt, S. F. L., Talling, P. J., Vardy, M. E., Masson, D. G., Henstock, T. J., Hühnerbach, V., Karstens, and J: Widespread and progressive seafloor-sediment failure following volcanic debris avalanche emplacement: Landslide dynamics and timing offshore Montserrat, Lesser Antilles, Marine Geology, 323, 69-94, doi: 10.1016/j.margeo.2012.08.002, 2012.

855   Winkelmann, D., Geissler, W., Schneider, J., and Stein, R: Dynamics and timing of the Hinlopen/Yermak Megaslide north of Spitsbergen, Arctic Ocean, Mar. Geol,, 250(1), 34–50, doi: 10.1016/j.margeo.2007.11.013, 2012.

Worsley, D., Aga, O.J., Dalland, A., Elverhøi, A., and Thon, A: The Geological History of Svalbard, Evolution of an Arctic Archipelago, Statoil, Asker Trykkeri, Stavanger, 121, 1986.

Zhang, W., Almgren, A., Beckner, V., Bell, J., Blaschke, J., Chan, C., and Zingale, M: AMReX: a framework for block-
860   structured adaptive mesh refinement, J. Open. Source. Softw., 4(37), 1370-1370, doi: 10.21105/joss.01370 , 2019.